Chinese Chemical Letters 36 (2025) 110466

Contents lists available at ScienceDirect

Chinese Chemical Letters

journal homepage: www.elsevier.com/locate/cclet

sp[1]-Hybridized linear and cyclic carbon chain

Huiju Cao, Lei Shi*

State Key Laboratory of Optoelectronic Materials and Technologies, Guangdong Basic Research Center of Excellence for Functional Molecular Engineering, Nanotechnology Research Center, School of Materials Science and Engineering, Sun Yat-sen University, Guangzhou 510275, China

ARTICLE INFO

Article history:
Received 12 July 2024
Revised 31 August 2024
Accepted 13 September 2024
Available online 16 September 2024

Keywords:
Linear carbon chains
Cyclo[*n*]carbons
Polyyne
Carbyne
Synthesis
Properties

ABSTRACT

Carbon materials have long been a subject of study, offering diverse properties based on their hybridized structures. Except sp[2]-hybridized graphene and carbon nanotubes, the focus on sp[1]-hybridized carbon chains has garnered significant interest due to its unique predicted properties, despite limitations in research and development stemming from its high reactivity. This comprehensive review summaries recent advancements in synthetic methodologies and characterization of the sp[1]-hybridized carbon chains, encompassing linear carbon chains and cyclo[*n*]carbons. The review traces significant milestones in synthesis and offers a thorough overview of various properties on linear and cyclic carbon chains, from their initial discovery to recent development. The advancing synthetic methods have led to practical breakthroughs, transitioning theoretical concepts into tangible carbon-chain materials. However, challenges persist in achieving controlled and scalable preparation due to the high reactivity associated with sp[1]-hybridization. Future research prospects focus on fundamental studies, such as exploring the transition length from polyyne to carbyne and experimentally determining the properties of single carbon chains. This review underscores both the progress made and the compelling avenues for future exploration in the dynamic field of sp[1]-hybridized carbon chains.

1. Introduction

Carbon, a ubiquitous and widely distributed element in nature, serves as an indispensable building block for life in various forms. Its versatility is evident as it can manifest in solid, liquid, gas, and other states of matter. The pivotal turning point in the exploration of novel allotropes of carbon occurred with the groundbreaking discovery of fullerene in 1985 [1], ultimately earning the Nobel Prize in Chemistry in 1996 (Richard F. Curl, Harold W. Kroto, and Richard E. Smalley). This discovery sparked a surge in research interest, propelling scientists to delve into the diverse realm of carbon materials. The subsequent discovery of carbon nanotubes (CNTs) by Sumio Iijima played a transformative role in advancing the exploration of synthetic carbon materials [2], further intensifying the fervor of researchers. Notably, the Nobel Prize in Physics in 2010 was awarded to Andre Geim and Konstantin Novoselov "for groundbreaking experiments regarding the two-dimensional material graphene" [3]. Fullerene, CNTs, and graphene, despite being well-established sp[2]-based allotropes, represent only a fraction of carbon's multifaceted forms. These discoveries have garnered widespread attention due to their unique structures and properties, subsequently playing a pivotal role in various applications. In contrast, the sp[1]-hybridized carbon chain, another intriguing carbon allotrope, has been under investigation for over a century, yet remains relatively obscure in scientific discourse. Recent strides in carbon chain research from various perspectives underscore its growing significance, warranting a comprehensive introduction to illuminate the noteworthy progress in this understudied domain.

The carbon materials can be systematically classified based on their hybridization into three primary types: sp^n (n = 3, 2, or 1) (Fig. 1) [4]. The sp[3]-hybridized mode is exemplified in diamond, encompassing derivatives such as C_8 and lonsdaleite. Graphite and graphene exhibit sp[2] hybridization, and its derivatives, including fullerenes and carbon nanotubes, fall under sp^n hybridization, where n is between 2 and 3 but closer to 2. A distinctive sp[1]-hybridized representative is carbon chain, which exists in various forms, *e.g.*, linear or cyclic carbon chains. Linear carbon chain (LCC) with infinite length is termed carbyne [5,6]. Theoretically, the strength, modulus of elasticity, stiffness, and thermal properties of carbyne surpass those of currently known carbon materials, including diamond, carbon nanotubes, and graphene [7]. Furthermore, polyynic carbon chain exhibits semiconductor behavior, wherein its energy gap can be modulated by both length and end-group configuration, further influenced by environmental factors such as

* Corresponding author.
E-mail address: shilei26@mail.sysu.edu.cn (L. Shi).

https://doi.org/10.1016/j.cclet.2024.110466
1001-8417/

Table 1
Classification of sp^1-hybridized carbon chains.

LCCs				Cyclo[*n*]carbons	
Polyyne	Cumulene	LCCs@CNTs	Carbyne	Polyynic	Cumulenic
Alternative single-triple carbon-carbon bonds	Successive double carbon-carbon bonds	LCCs encapsulated in CNTs with polyynic structure	Infinite carbon chains or the property does not rely on its length	Alternating single-triple carbon-carbon bonds	Successive double carbon-carbon bonds
Semiconducting	Metallic	Semiconducting	Semiconducting or metallic	Semiconducting	Metallic

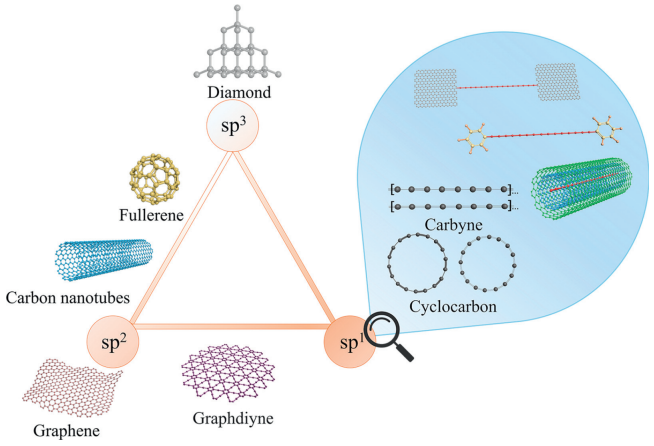

Fig. 1. Allotropes of carbon classified by electron orbital hybridization.

solvent, substrate, and template. Therefore, sp^1-hybridized carbon chains are at the forefront of research, and their exceptional material properties are poised to make them the new frontrunner in the field of carbon nanomaterials.

In this comprehensive review, we aim to systematically organize and elaborate on the latest research pertaining to sp^1-hybridized carbon chains, with a primary focus on their synthesis and properties. Our approach begins with an introduction to sp^1-hybridized carbon chains, specifically delving into LCC and cyclo[*n*]carbon. Subsequently, we delve into a detailed examination of the structures and experimental findings related to the synthesis of polyyne, LCCs inside carbon nanotubes (CNTs), and cyclo[*n*]carbons. Finally, we discuss the properties and feasible applications inherent in LCCs and cyclo[*n*]carbons, providing an overview of the current state of knowledge in the field.

2. Classification of sp^1-hybridized carbon chains

While ongoing research on sp^1-hybridized carbon chains remains in a phase of continuous exploration, it is evident that sp^1-hybridized carbon structures primarily encompass LCCs (both finite and infinitely long) and cyclo[*n*]carbons. Early efforts to understand the structure of sp^1-carbon materials mainly involved theoretical predictions. In 1966, Hoffman [8] conducted extended Hückel rule calculations on linear and cyclo[*n*]carbons (n=4-18), determining that the linear chain structure is more stable when $n < 10$, while the cyclic structure becomes more stable when $n > 10$ [9]. However, experimentally much longer LCCs have been successfully synthesized (*e.g.*, polyynes comprising 44, 48, 52, and 68 carbon atoms and LCC consisting of more than 6000 carbon atoms in CNTs) [10-14], but only small cyclo[*n*]carbon molecules (*e.g.*, with 10, 13, 14, 16, 18 and 26 carbon atoms) [15-18] were synthesized. The classification of sp^1-hybridized carbon chains was succinctly outlined in Table 1.

The ideal LCC is an infinitely long structure or, when its properties remain unaltered with length, is termed carbyne. However, synthesis of carbyne poses challenges due to its super-active nature. The properties of carbyne, such as exceptional mechanical and photothermal characteristics, were mostly predicted based on infinitely LCC, *i.e.*, carbyne. Experimentally, these properties were examined by preparing the longest achievable carbon chains. Remarkably, carbon chains exceeding 6000 atoms were synthesized inside CNTs, known as LCC@CNT, establishing a record for laboratory-prepared carbon chain length [14]. Significantly, the properties of the LCC inside CNT were found to be independent of LCC's length, marking it as the first experimentally confirmed carbyne, which was termed confined carbyne (CC), because it only existed in confined environment of the CNT. Beyond LCC, cyclo[*n*]carbons emerge as another distinct class of sp^1-hybridized carbon chains. These structures are composed of rings formed by doubly coordinated carbon atoms. The properties of cyclo[*n*]carbons are notably influenced by the number of carbon atoms within the rings. Understanding the variations in properties corresponding to different carbon atom counts in these cyclic structures is crucial for comprehending the diverse characteristics and potential applications of the cyclo[*n*]carbons in the realm of sp^1-hybridized carbon materials. Up to know, six types of cyclo[*n*]carbons structures have been observed and confirmed in experiments: n = 10, 13, 14, 16, 18, 26 [15-18]. Among them, cyclo[10]carbon has cumulenic structure, cyclo[14]carbon has cumulene-like structure, and cyclo[16,18]carbon possess polyynic structure [16]. Further research is likely to shed light on the specific properties and behaviors associated with cyclo[*n*]carbons of varying sizes, contributing to the broader understanding of sp^1-hybridized carbon materials and their applications.

2.1. LCCs

LCCs encompass polyyne, cumulene, LCCs@CNTs, and carbyne [6,19], as outlined in Table 1. These structures can be also classified based on the different types of chemical bonds present in the carbon chain. Bond length alternation (BLA) between the single bond and triple bond of carbon atoms can be used to clarify two types of structures: polyynic, characterized by alternating C-C and C≡C bonds following Peierls distortion theory (BLA≠0), and cumulenic, featuring a continuous C=C bonds structure (BLA = 0). Occasionally, polyyne is named as α-carbyne, while cumulene is referred to as β-carbyne [20]. Polyyne typically refers to a class of LCCs, where the simplest form of polyyne, terminated with hydrogen, can be represented as C_nH_2. LCCs normally exhibit high reactivity, and their structures are inherently unstable. Exposure to oxygen and humidity can lead to decomposition or cross-linking reactions, resulting in the formation of other structures. Consequently, LCCs find it challenging to exist independently at ambient conditions [21]. *Ab-initio* theoretical calculations suggested that polyyne has better stability compared to cumulene [22]. Experimental evidence further supports the higher stability of polyyne compared to cumulene. For instance, when two carbon chains of the same length

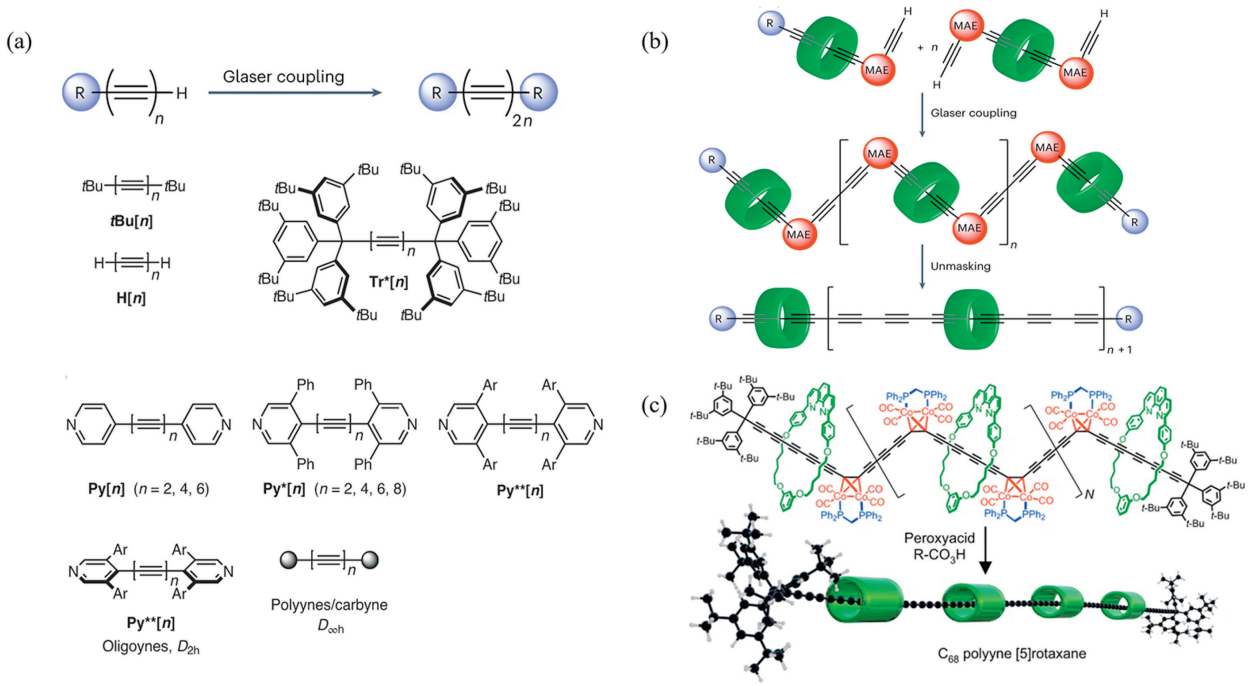

Fig. 2. Strategies for synthesizing long polyynes. (a) Conventional approaches to synthesize polyynes with various end groups [11,13]. Copyright 2020, Springer Nature. (b) In the precursor polymer route, the masked acetylene equivalents conceals the reactivity of alkynes until the entire backbone has been constructed. (c) Strategy for the synthesis of C_{68}[5]rotaxane with 34 contiguous triple bonds [13]. Copyright 2023, The Author(s).

are prepared, polyyne can be dried and preserved as solid, while cumulene can only be preserved in solvent [23,24]. In contrast, confinement within CNTs helps maintain the structural integrity of LCCs, making it a more stable form of LCC material. These stability considerations are crucial for understanding the practical feasibility and potential applications of different LCC structures.

2.2. Cyclo[n]carbons

Cyclo[n]carbons represent another fascinating allotrope of carbon formed through sp^1-hybridization. These are all-carbon rings characterized by two orthogonal π systems, typically with n electrons in each system. The classification of cyclo[n]carbons involves two main groups: $n = 4m + 2$ and $n = 4m$ (where n is a positive integer). The concept of cyclo[n]carbons was initially introduced by Pitzer and Clementi in 1959, and it is predicted that molecules with $n = 4m + 2$ will exhibit particular stability [25]. The cyclo[n]carbons can be further categorized based on the two structures of the sp^1-hybridized carbon chain: polyynic and cumulenic (Table 1). These structural variations contribute to the diversity of cyclo[n]carbons, offering intriguing possibilities for different properties and behaviors.

3. Synthesis of sp^1-hybridized carbon

The inherent instability and high chemical reactivity associated with sp^1-hybridized structures limit the laboratory preparation of LCCs. Nonetheless, researchers persistently investigated these structures owing to their potentially exceptional properties. The primary focus centers on synthesizing polyyne with increasing length, as the double bond form of cumulenes is excessively unstable [22]. Various methods have been developed to obtain longer polyynes with the ultimate goal of achieving carbyne. Additionally, recent studies on cyclo[n]carbons have raised considerable interest in this type of carbon chains. The principal methods employed for the preparation of both LCCs and cyclo[n]carbons are outlined in the subsequent sections.

3.1. Preparation of carbon chains

3.1.1. Organic chemical synthesis of polyynes

The bottom-up strategy in organic chemical synthesis involves stabilizing carbon chains through the introduction of diverse end groups, which encompass alkyl, aryl, trialkylsilyl, and even organometallic groups. Primary molecular structures of reported end-capped long polyynes are present in Fig. 2a. The foundational synthetic approach for polyynes is rooted in the Glaser reaction [26]. However, the initial application of the Glaser reaction was limited. To address this, the Eglinton-Galbraith and Hay reactions were developed to modify the Glaser reaction for the synthesis of polyynes [27]. These reactions were employed to create functionalized polyynes through homocoupling reactions.

Initially, the synthesis of short polyynes with $n < 20$ carbon atoms was achievable, but the polyynes was preserved in dilute solutions. Upon solvent removal, rapid polymerization occurred, and the yield diminished with increasing chain length [28]. In the early 1950s, Bohlmann and colleagues implemented an elimination strategy to synthesize *tert*-butyl-end-capped polyynes [29]. This end group demonstrated a protective role by circumventing unstable precursors and products. Subsequently, chemists focused on synthesizing various end-groups, including asymmetric polyynes generated through heterocoupling protocols [30].

As synthesis methods advanced, researchers discovered that large and sterically demanding end-capped groups allowed synthetic access to significantly longer polyynes, maintaining stability in both solution and the solid state. Chalifoux *et al.* utilized the tris methyl moiety (3,5-di-*tert*-butylphenyl, Tr*) to synthesize polyynes with 44 carbon atoms [10]. Later, they achieved longer polyyne, comprising 48 carbon atoms, featuring the *t*Bu pyridyl group [11]. Recently, PtCnSi structured polyynes were extended by using the mutable structural unit HC_8Si, resulting in the formation of a new

Table 2
Various polyynes with different end-groups synthesized by organic chemical synthesis.

Type of end-group	Product	Maximum number of carbon atoms (n)	Type of reactions
Asymmetric end-capped	PtF[n]Si, Pt[n]Si [12], BF[n]Si, BF_2[n]Si(iPr)$_3$;	32	Oxidative heterocouplings, heterocoupling reactions
Sp^3-carbon end-capped	Tbu[n], Ad[n], Tr*[n] [10], Glu[n]	44	Eglinton-Galbraith coupling, Elimination reaction, desilylation reaction
	Tr*M_1[n], Tr*M_2[n] [13]	68	Masked acetylene equivalents, Eglinton-Galbraith; Glaser reaction, desilylation reactions, Cadiot-Chodkiewicz reactions
Sp^2-carbon end-capped	Py*[n], Ph[n], ArOsi[n], PhF[n], Dend[n], Py[n], BF[n], $PhNH_2$[n], BT[n], Py**[n] [11], $PhCF_3$[n]	48	Oxidative acetylenic coupling reactions, Eglinton-Galbraith conditions, Hay reaction
Metal-end-capped polyynes	Ru[n], RuRu[n], Re[n], TIPS[n], Pt[n] [12], PtT[n], PtF[n], CoC[n], TES[n], PtC[n], Co_3C[n]CCO_3	52	Oxidative heterocouplings, Hay reaction, heterocoupling reactions

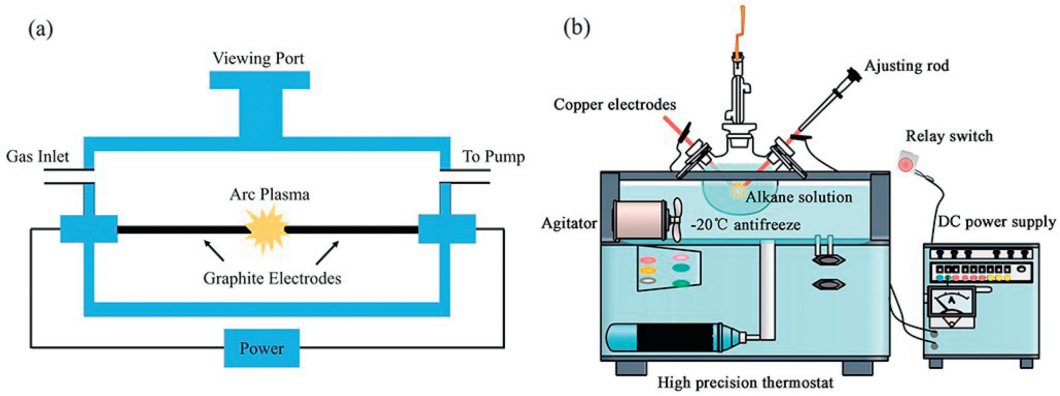

Fig. 3. (a) Schematic representation of an arc-discharge apparatus. (b) Preparation of polyynes by arc discharge method in solvent [43]. Copyright 2019, Elsevier.

platinum polyynediyl complexes from $PtC_{28}Pt$ up to $PtC_{52}Pt$ [12]. Not only the length of the polyyne, but also the type of the end-groups greatly affects the properties of polyynes. The effect of end groups decreased when the polyyne lengthened. However, a crucial question remains: will the end-group effect completely disappear? This inquiry stands as a key exploration point in understanding the nature of carbyne, captivating researchers' continuous efforts.

A novel proposition to enhance the stability of polyynes involves threading them through macrocycles to form rotaxanes or polyrotaxanes [31]. This approach, utilizing masked acetylene equivalents and protective strategies for the polyynes (Fig. 2b). Movsisyan *et al.* showcased the preparation of polyyne rotaxanes through active-metal templating, employing a phenanthroline-based macrocycle [32]. Their work demonstrated successful synthesis with carbon chain lengths up to 20 atoms, suggesting the potential as a robust method for controlling the environment around polyyne chains. The initial exploration of odd[9]cumulene involved the synthesis of cumene rotaxane M1·[9]$t$$Bu_2$Ph [33]. More recently, Patrick *et al.* [34] presented a groundbreaking method where masked alkynes, with the C≡C triple bond temporarily coordinated to cobalt, were utilized to synthesize polyrotaxanes (Fig. 2c). The resulting C_{68}[5]rotaxane featured 34 contiguous triple bonds and four threaded macrocycles, setting a new record for the length of polyynes prepared by chemical synthesis. This advancement extended the record from 52 to 68 carbon atoms [11,13]. In fact, the types of polyacetylene end groups prepared by chemical synthesis are very rich. The most common types of end groups are summarized in Table 2.

3.1.2. Arc discharge method

Arc discharge method has been a key technique for the preparation of carbon nanotubes [35] and fullerenes [36]. It involved using graphite rods in a leak-tight cavity or in solvents, where the graphite poles served as the cathode and anode, as shown in Fig. 3a. Generally inert gas is used as a protective gas during the arc discharge process [37-39]. Similarly, significant quantities of polyyne mixtures could be synthesized in solvents, such as methanol, acetonitrile, or *n*-hexane, using arc discharge method. By controlling different solvents, polyynes with hydrogen-capped and cyanide-capped groups were obtained [40,41]. The lengths of the synthesized polyynes typically ranges from 6 to 24 carbon atoms [42]. Later, as shown in Fig. 3b, improvements were made to the arc discharge method, including the use of different electrode materials (*e.g.*, copper electrodes in alkanes) and alternative solutions (*e.g.*, graphite electrodes in pure water) [43,44]. While these enhancements did not result in significant breakthroughs in the length of carbon chains, they did contribute to improving the efficiency of prepared materials [45].

In 2003, a significant breakthrough was achieved when the presence of a LCC was discovered inside the most-inner tubes of MWCNTs in the cathode deposits generated through arc discharge evaporation of carbon rods in hydrogen atmosphere [46]. The LCCs consist of around 100 carbon atoms, which is already longer than any polyyne synthesized by organic chemical synthesis and arc-discharge method in solvents. Later, LCCs were also observed when preparing MWCNTs using the arc discharge technique within a helium atmosphere [47]. Combination of high-resolution transmission electron microscopy (HRTEM) and Raman spectroscopy allow to study LCCs inside MWCNTs [46,48].

3.1.3. Laser ablation in liquids

Laser ablation in liquids (LAL) is a technique that creates ultra-high temperature and ultra-high pressure environments in liquids, providing a unique pathway for the preparation of nanomaterials [7,49]. In the context of polyyne synthesis, LAL has been employed to directly generate polyynes, which is similar to the arc-discharge in solvents. Polyynes with an even number of carbon atoms ranging from 8 to 16 were formed by laser ablating graphite particles

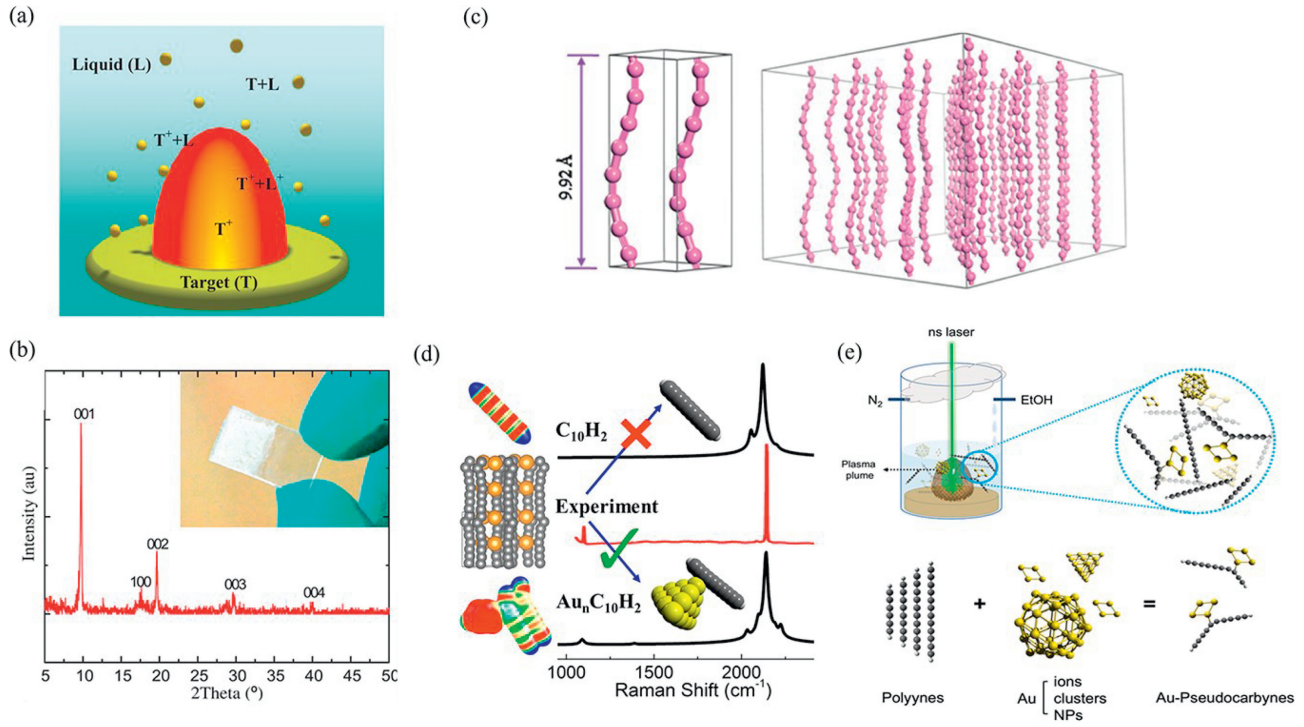

Fig. 4. (a) Schematic diagram of synthesis mechanism of polyynes by LAL. (b) Morphology and XRD of polyyne crystals. (c) Molecular structure of a polyyne crystal [57]. Copyright 2015, American Association for the Advancement of Science. (d) Raman spectra of Au-pseudocarbyne prepared by different methods [58]. Copyright 2016, American Chemical Society. (e) Schematic diagram of synthesis of Au-pseudocarbynes *via* LAL (top) or self-assembly (bottom) [59]. Copyright 2018, the Royal Society of Chemistry.

suspended in benzene, toluene, or hexane [50]. The mechanism of polyyne formation in this process involves the consecutive coupling reaction of C_2 radicals produced by laser ablation. The growth is then terminated by the addition reaction of hydrogen atoms from solvent molecules at both ends of a polyyne molecule. The length of the polyyne chain depends on the number density of C_2 radicals and the ratio of hydrogen atoms in the solvent molecule. Kojima *et al.* extended the application of liquid-phase laser ablation to *n*-hexane, achieving the synthesis of polyynes up to $C_{22}H_2$ [51,52]. Also, they reported the synthesis of long polyynes from graphite pellets in a decalin solvent. In this case, the termination reaction on both ends of the polyyne molecule hardly occurred in decalin due to its relatively smaller ratio of hydrogen atoms, resulting in the production of long-chain polyynes such as $C_{24}H_2$ and $C_{26}H_2$ [53]. By utilizing a laser with a wavelength of 1064 nm, they further extended the synthesis of polyynes consisting of up to 30 carbon atoms [53,54]. This method showcases the versatility of the LAL for controlled and efficient synthesis of long polyynes. The synthesis in general is influenced by factors such as solvent, pulse duration, laser wavelength, and energy of the laser beam [55]. Recent study showed that size- and solvent-dependent production rates of polyynes are influenced by the solvent's C/H ratio. However, a long ablation in a small volume of solvent cannot achieve polyynes with a high concentration [56].

Synthesis of polyyne nanocrystals was achieved using the LAL [57]. A solution containing polyynes was obtained by ablating a gold target immersed in an alcoholic solution with laser pulses (Fig. 4a). The solution was then purified using high-performance liquid chromatography, and the polyynes were subsequently isolated. Polyyne crystals were formed after the solution was dried. The quality and crystallinity of the synthesized polyyne crystals were confirmed through X-ray diffraction (XRD), with the diffraction pattern of the sample displaying clean, well-shaped, and strong peaks, indicative of good crystallinity (Fig. 4b). Additionally, the equilibrium configuration of the constructed polyyne nanocrystals was proposed through first principles calculations, providing a deeper understanding of their structural characteristics (Fig. 4c). *Ab initio* calculations revealed that the electron densities of the C≡C bonds in the polyynes were dramatically altered by the presence of gold clusters (Fig. 4d) [58]. This change in electron density leads to charge stabilization, resulting in structures termed pseudocarbyne. Therefore, it was suggested by Buseck *et al.* that the material synthesized and characterized by Pan *et al.* [57] might be more consistent with the presence of C/Au clusters rather than pure polyyne nanocrystals. This implies that the observed structures were influenced by the interaction with gold clusters. Subsequently, further experiments were conducted, and derivative pseudocarbynes were synthesized using a more straightforward self-assembly method compared to previous approaches [59]. In this method, polyynes assembled with Au clusters at ambient conditions, forming Au-pseudocarbyne (Fig. 4e). The formation of the Au-pseudocarbyne product was confirmed through spectroscopic characterization. This work shed light on the role of gold clusters in influencing the properties and structures of polyyne nanocrystals, expanding the understanding of carbon-gold interactions in nanomaterial synthesis [58,59].

3.1.4. On-surface synthesis

On-surface synthesis was employed to investigate the reaction of ethylene on the Cu(110) surface (Fig. 5a), resulting in the generation of metalated carbynes capable of modulating the intrinsic physicochemical properties of carbon nanomaterials [60,61]. Acetylene was chosen as the precursor molecule, and experimental conditions were optimized by adjusting the substrate temperature to prevent unnecessary side reactions while promoting the dehydrogenation coupling reaction. Notably, metalated carbyne of submicron lengths were achieved, with the longest chains measuring up to 120 nm [62]. Subsequently, the fabrication of organometallic polyyne (-C≡C-C≡C-Au-)n was reported (Fig. 5b), utilizing the precursor $Br_2C{=}C{=}C{=}CBr_2$ on Au(111) [63]. The cumulene moiety

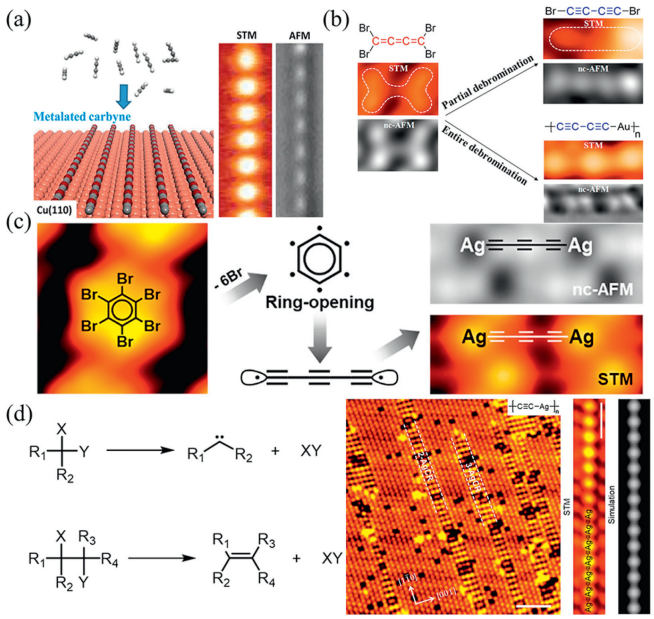

Fig. 5. On-surface synthesis of (a) Cu-carbyne [62], Copyright 2016, American Chemical Society. (b) Au-carbyne [63]. Copyright 2020, American Chemical Society. (c) Ag-carbyne [64]. Copyright 2022, American Chemical Society. (d) Metalated carbyne ribbons [65]. Copyright 2023, American Chemical Society.

($Br_2C{=}C{=}C{=}C{=}CBr_2$) underwent a rearrangement of the molecular backbone from cumulene to diyne moiety (Br-C≡C-C≡C-Br) under STM tip manipulation. Through a surface reaction strategy, thermally induced debromination (:C=C=C=C=C:) led to the organometallic polyyne. Electronic property measurements of the prepared metalated carbyne revealed a semiconducting characteristic [63]. In addition, elimination of bromine atoms from hexabromobenzene (C_6Br_6) molecules on Ag(111) substrate *via* heat treatment facilitated the conversion of dibrominated molecules through ring-opening process into polyyne chains, ultimately polymerizing into organometallic polyynes (Fig. 5c) [64]. Metalated carbyne ribbons containing Cu or Ag atoms were also formed through the elimination reaction of tetrabromomethane (CBr_4) and hexabromoethane (C_2Br_6) on the surface [65]. Debromination elimination reactions were performed on Ag (110), followed by polymerization to create metalated carbyne ribbons (Fig. 5d). Density functional theory (DFT)-calculated spin-polarized density of state (DOS) analyses indicated that the bandgap decreases with an increase in the width of metalated carbyne ribbons. Remarkably, LCC consisting of 60 alkyne units, *i.e.*, 120 carbon atoms, was synthesized on the surface of Au(111) by demetallization of organometallic polyynes, which is the longest free-standing LCC on substrate so far [66].

3.1.5. Carbon chains converted from other carbon materials

Carbon chains converted from other carbon materials have been achieved through an *in-situ* synthesis technique, relying on HRTEM to form carbon chains by stripping carbon nanomaterials using a controlled electron illumination-assisted technique. Irradiation of single-walled carbon nanotubes (SWCNTs) results in failure of the SWCNTs and formation of a short single carbon chain before breaking down (Fig. 6a). Similarly, formation of short carbon chains was observed by irradiating graphene with electron beams in a HRTEM (Fig. 6b) [67]. Moreover, when the portion of the sample in contact with the tip started to disconnect from the larger sheet, a graphite structure with a width of less than 1 nm formed between the two regions (Fig. 6c). Further separation of the tip from the sample resulted in the stretching of the graphene structure and eventually the unravelling of carbon chains from the graphene layer. The conductivity of the free-suspending carbon chains was characterized. Although carbon chain had a short life and the measurement of current is affected by noise, it still exhibited obvious non-ohmic behavior [68].

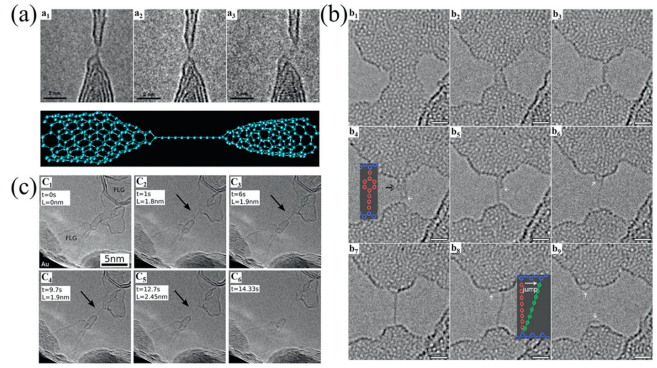

Fig. 6. (a) HRTEM images and a molecular model of a carbon chain formed from a CNT [69]. Copyright 2003, American Chemical Society. (b) Consecutive HRTEM images of formation and breakage of freestanding carbon chains through continuous electron beam irradiation on graphene [67]. Copyright 2009, American Physical Society. (c) *In-situ* extraction of a carbon chain from graphene under HRTEM [68]. Copyright 2013, American Chemical Society.

3.1.6. Confined synthesis

Carbon nanotubes were employed as nanoreactors for the synthesis of carbon materials. In principle, their 1D hollow structure can provide a suitable environment for the growth of LCCs [70-72]. As discussed above, LCCs were formed simultaneously with MWCNTs during arc-discharge process (Fig. 7a) [46,47]. In fact, post treatment was also proved as an effective method to synthesize LCCs inside CNTs. In 2011, LCCs were obtained by fusion reactions between polyynes ($C_{10}H_2$) in DWCNTs (Fig. 7b) [73]. The LCCs were estimated to consist of ~50 carbon atoms. Subsequently, theoretical calculations suggested the thermal transformation of LCC@CNTs by annealing of adamantane molecules encapsulated in a CNT. It is also found that carbon chains are very stable in a CNT with an inner diameter of about 1.0 nm, while CNTs with an inner diameter of more than 1.3 nm tend to contain multiple carbon chains [74]. In 2016, a high-temperature annealing method was used to synthesize ultra-long LCCs in narrow DWCNTs. As shown in Fig. 7c, a LCC was clearly observed inside a DWCNT [14]. This strategy resulted in LCCs containing more than 6000 carbon atoms affirmed by tip-enhanced Raman spectroscopy, which is still the current record for the longest LCCs. Furthermore, it is possible to extract the LCCs together with the inner tubes from the hosting outer tube of DWCNTs, thus LCCs@SWCNTs were obtained [75].

Utilization of SWCNTs as nanoreactors for the preparation of LCCs can also be realized (Fig. 7d) [76]. However, due to small diameter and susceptibility to defects during the preparation process, the formation efficiency of LCCs is limited using SWCNTs. In 2006, a hybrid material of $C_{10}H_2$@SWCNTs was obtained by incorporating chromatographically purified $C_{10}H_2$ into SWCNTs [77]. In 2021, LCCs@SWCNTs were prepared through a controllable fusion reaction of polyynes inside thin SWCNTs [78]. In 2019, an alternative approach to produce LCCs was achieved, involving field electron emission accompanied by electrical discharge from SWCNT films [79]. The results demonstrated the formation of LCCs inside both SWCNTs and DWCNTs. For the DWCNTs with an inner diameter of 0.7 nm, the LCCs were found to lie directly along the central tube axis. In SWCNTs with an inner diameter of 1.0 nm, the encapsulated LCCs were observed to be bent and positioned close to the nanotube wall, thus away from the central tube axis, as shown in Fig. 7d.

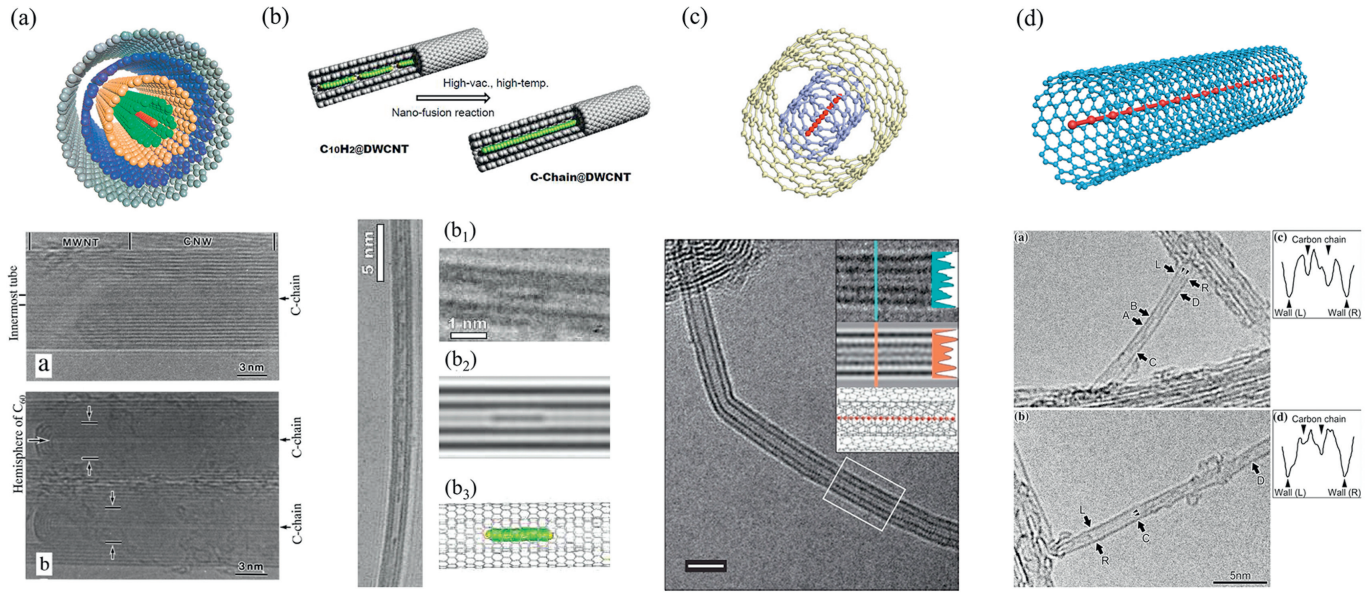

Fig. 7. Molecular structures and HRTEM images of LCCs inside various CNTs. (a) LCCs@MWCNTs [46]. Copyright 2003 American Physical Society. (b) polyynes@DWCNT [73]. Copyright 2011, American Chemical Society. (c) LCC@DWCNT [14]. Copyright 2016, Springer Nature. (d) LCCs@SWCNTs [79]. Copyright 2019, Springer Nature.

3.2. Preparation of cyclo[n]carbons

3.2.1. Early attempt at synthesis of cyclo[n]carbon

Laboratory preparation of cyclo[*n*]carbon is divided into two routes, with one involving the vaporization of graphite to produce carbon clusters, and the other relying on molecular precursors [80]. Carbon clusters from graphite vaporization are mainly associated with high-temperature methods, such as laser ablation, to yield carbon clusters containing both linear and cyclic isomers. However, short polyynes typically prevail, accompanied by fewer cyclic isomers [81]. The structure of cyclo[*n*]carbon generated through this vaporization process is inherently unstable and exists only in the gas phase, limiting its structural observation [82,83]. In addition, attempts were made to synthesize cyclo[*n*]carbon through chemical methods.

In 1989, the first attempt to synthesize cyclo[*n*]carbon was achieved, employing a cyclic precursor based on an anthracene-masked alkyne equivalent and monitoring cyclo[18]carbon through time-of-flight mass spectrometry [84]. Over the ensuing decade, various reactive precursors (*e.g.*, cyclo[*n*]carbon oxide precursor, propellane-annulated dehydroannulene, and others) were designed for cyclo[*n*]carbon synthesis [85-87]. In 2003, Tobe *et al.* prepared epoxide precursors of cyclo[18]carbon, cyclo[24]carbon, cyclo[36]carbon and analyzed them by mass spectrometry [86]. Although it was still not possible to successfully isolate the cyclo[*n*]carbon, this lays the foundation for subsequent studies on the preparation of molecular precursors. Selective production was achieved using designed precursors, and the resulting cyclo[*n*]carbon species proved too reactive to be isolated under ambient conditions [34,80,88].

3.2.2. On-surface synthesis of cyclo[n]carbon

Great breakthroughs have been made in the preparation of cyclo[*n*]carbon by surface synthesis in recent years. As shown in Table 3, we have statistically sorted out the synthesized cyclo[*n*]carbon in recent years. In 2019, researchers confirmed the polyynic structure of cyclo[18]carbon [18]. The on-surface synthesis opens up a route for synthesis and direct observation of various cyclo[*n*]carbons.

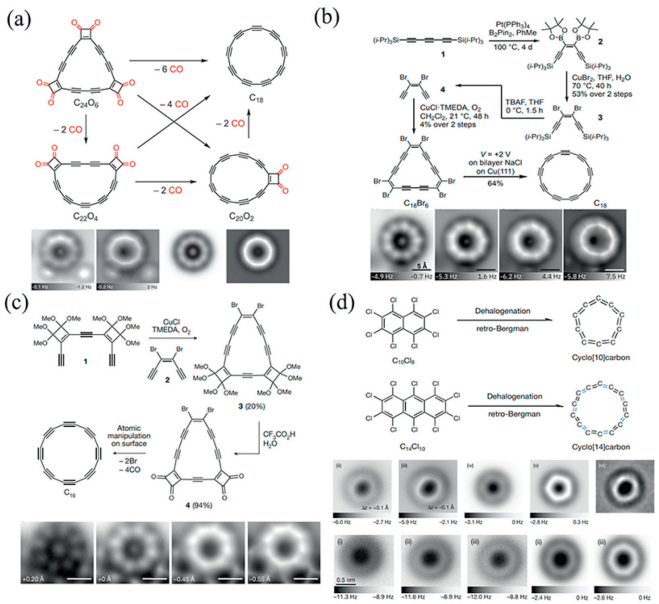

Fig. 8. Reaction schemes for the formation of cyclo[*n*]carbon (top) and corresponding AFM images (bottom): (a) cyclo[18]carbon [18]. Copyright 2019, American Association for the Advancement of Science. (b) cyclo[18]carbon [89]. Copyright 2020 American Chemical Society. (c) cyclo[16]carbon [17]. Copyright 2023, The Author(s). (d) cyclo[10]carbon and cyclo[14]carbon [16]. Copyright 2023, Springer Nature.

As shown in Fig. 8a, cyclo[18]carbon was generated through atom manipulation on bilayer NaCl on Cu(111), where carbon monoxide was eliminated from $C_{24}O_6$ as the precursor molecule [18]. A polyynic structure for cyclo[18]carbon with defined positions of alternating triple and single bonds was revealed through high-resolution atomic force microscopy. Subsequently, a high-yield approach to preparing cyclo[18]carbon was achieved by using a bromocyclocarbon precursor, *i.e.*, $C_{18}Br_6$ [89]. $C_{18}Br_6$ was debrominated on a double layer of NaCl on Cu (111), resulting in the formation of cyclo[18]carbon in a 64% yield (Fig. 8b), which was 5 times greater than that from $C_{24}O_6$ precursors. Using the same strategy, researchers subsequently obtained cyclo[16]carbon

Table 3
Synthesis and structure of cyclo[*n*]carbon.

Precursor molecule	The number of carbon atoms (*n*)	Structure	Synthesis method
$C_{10}Cl_8$	Cyclo[10]carbon [16]	Cumulenic	Dehalogenation, Retro-Bergman, Atom manipulation
$C_{13}Cl_{10}$	Cyclo[13]carbon [15]	Polyynic	Dehalogenation, Retro-Bergman, Atom manipulation
$C_{14}Cl_{10}$	Cyclo[14]carbon [16]	Between cumulenic and polyynic	Dehalogenation, Retro-Bergman, Atom manipulation
$C_{16}(CO)_4Br_2$	Cyclo[16]carbon [17]	Polyynic	Atom manipulation, Remove masking CO groups, Dehalogenation
$C_{24}O_6$ or $C_{18}Br_6$	Cyclo[18]carbon [18,89]	Polyynic	Atom manipulation, Remove masking CO groups or dehalogenation
$C_{13}Cl_{10}$	Cyclo[26]carbon [15]	Polyynic	Atom manipulation, Dehalogenation, Dimerization

on surface. Fig. 8c shows the synthesis and characterization of cyclo[16]carbon through tip-induced on-surface chemistry using $C_{16}(CO)_4Br_2$ as precursor [17]. Cyclo[16]carbon exhibited a polyynic structure with alternating bond lengths as the cyclo[18]carbon. As mentioned earlier, on-surface synthesis of cyclo[16]carbon and cyclo[18]carbon by atom manipulation requires suitable precursor molecules. Other cyclo[*n*]carbons were then synthesized using different precursors [17,18]. Cyclo[10]carbon and cyclo[14]carbon were prepared on the bilayer NaCl/Au(111) surface (Fig. 8d). A cumulenic structure for cyclo[10]carbon was suggested, whereas cyclo[14]carbon was identified as an intermediate structure between the cumulenic cyclo[10]carbon and the polyynic cyclo[16]carbon. Albrecht *et al.* used voltage pulses from a scanning tunneling microscope tip to achieve the synthesis of cyclo[13]carbon by removing the chlorine atoms from decachlorofluoren. Interestingly, it was also showed that two cyclo[13]carbon molecules can be fused into a cyclo[26]carbon [15]. Although many progresses have been made in the preparation of cyclo[*n*]carbon, it is still lack of other method except AFM/STM for precision and large-scale synthesis.

4. Properties of sp[1]-hybridized carbon chains

4.1. Properties of LCCs

Investigation of substance properties plays a crucial role in determining its practical applications. Remarkable anticipated properties of carbon chains have generated significant interest in research efforts. In the subsequent section, we concentrate on exploring the electrical, mechanical, and optical properties, as well as environmental impact on various carbon chains.

4.1.1. Electrical properties

Various properties of carbyne were predicted through theoretical calculations. The band gap, a crucial parameter for investigating its electrical properties, was explored. The calculated energy band structures illustrate that the cumulene with two degenerate half-filled π-bands exhibits metallic characteristics (Fig. 9a). In contrast, for polyyne, the introduction of two electrons to each orbital, along with a half Brillouin zone, induces a separation in the conduction band, highlighting its semiconductor properties (Fig. 9b) [90]. BLA serves as a vital parameter describing the carbon chain structure [90,91]. The cumulene proves to be unstable in response to a change in BLA, transitioning to an alternated, polyynic configuration that corresponds to the minimum energy state. This transition by the potential energy curve is plotted against BLA, as determined through quantum chemical calculations (Fig. 9c). DFT calculations further suggest that cumulene represents a transition state within a thermodynamically driven structural evolutionary process [92].

Following the Peierls distortion theory [1,96], polyyne structure exhibits a non-zero BLA, and its BLA does not converge to zero with an increasing number of carbon atoms (Fig. 9d). In contrast, cumulene maintains a BLA of zero and remain constant as the atomic number increases. BLA significantly influences the electronic structure of the LCC, resulting in alterations to the band gap, which changes as a function of the BLA [93]. As the length

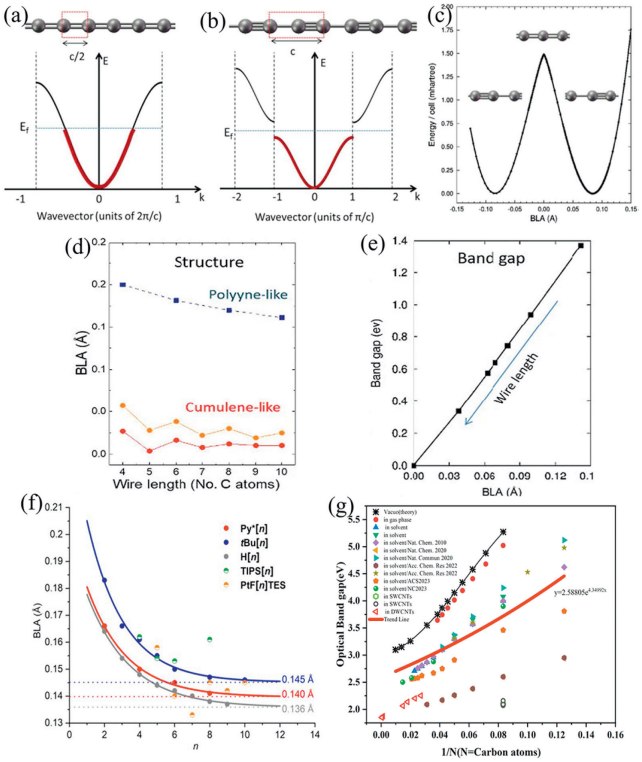

Fig. 9. The band structures of (a) cumulene and (b) polyyne. (c) Potential energy surface of an isolated infinite LCC as a function of BLA [90]. Copyright 2016, Royal Society of Chemistry. (d) DFT computed BLA values for LCC with polyynic or cumulenic structures. (e) Evolution of the band gap for finite LCC as function of BLA [93]. (f) Convergence of experimental BLAavg values as a function of the number of carbon atoms (n) of carbon chains [94]. Copyright 2022, American Chemical Society. (g) The relationship between the band gaps of LCCs and reciprocal number of carbon atoms in different environments [95]. Reproduced 2017, American Physical Society.

of the LCC increases, the BLA decreases, inducing changes in the electronic structure and ultimately leading to a reduced band gap (Fig. 9e). The band gap of infinite LCC in vacuum falls within the range of 8.5-2.0 eV, as obtained by various theoretical calculation methods [97,98]. However, for finite-length carbon chains, the band gap size varies with factors such as chain length, capping group, and environment, thereby allowing for regulation of the band gap [99,100]. Notably, even with regulation, the band gap of polyyne remains nonzero [101]. The BLA versus the number of carbon atoms for polyynes with different end-groups prepared by organic synthesis strategy is plotted in Fig. 9f, showing the BLA value decreases with the increase of the chain length [94]. At the same length, the BLA varies with the different end-groups, and they all converge to a constant value eventually [94].

Experimentally, the band gaps for end-capped polyynes containing 4-52 carbon atoms were reported in the range of 4.7-2.0 eV [10-12,100,102], which was well summarized in [103]. For LCCs synthesized inside DWCNTs, their band gaps range from 2.25 eV to

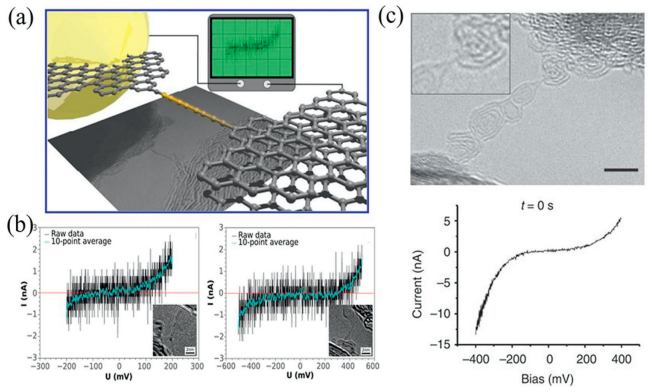

Fig. 10. TEM image/schematic diagram (a) and (b) Current-voltage curves of *in-situ* conductance measurement of a short LCC between graphene [68]. Copyright 2013, American Chemical Society. (c) TEM image and corresponding *I-V* curves of a strained short LCC [112]. Copyright 2015, The Author(s).

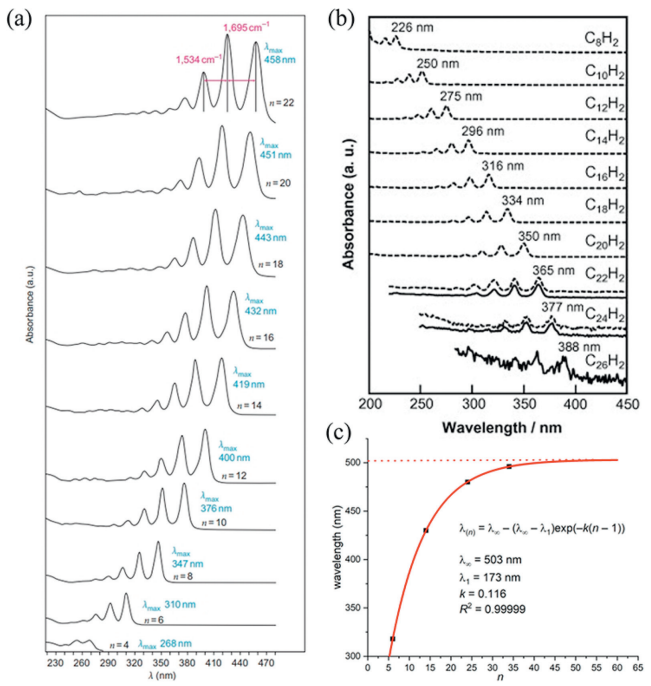

Fig. 11. (a) Absorption spectra of polyynes with Tr* end group (n = 4-18) [10]. (b) absorption spectra of hydrogen-capped polyyne in decalin solution [53]. Copyright 2010, Elsevier Ltd. (c) A plot of absorption wavelength of the absorption maximum λmax as a function of molecular length [13]. Copyright 2023, The Author(s).

1.85 eV [104]. In addition, LCCs inside CNTs have an overall lower band gap value compared to the freestanding polyynes. The relationship between the reciprocal number of carbon atoms and the band gap was across different environments (gas phase, solution, and carbon nanotubes) reveals significant influence from the environment, with band gaps potentially varying by up to 1 eV for LCCs of the same length. This is due to the fact that when the LCCs are inside the CNTs, the interaction and charge transfer occur between the LCCs and the CNTs, resulting in a decrease in the band gap [105].

Substitutional doping of heteroatoms is a common technique used to modify the electronic properties of carbon materials [106,107]. This technique can also induce changes in the energy gap of the LCCs. Theoretical investigations reveal that N doping significantly alters the gap of polyynes, with the gap being largely dependent on the position of the N atom within the polyyne structure [108]. This method of modulating the electronic properties of polyynes through N doping holds promise for future applications of polyynes as an N-type semiconductor.

Conductivity testing for LCCs poses challenges, as they differ from two-dimensional materials that can be measured on an area basis [109,110]. However, advancements in precision instruments have enabled the application of TEM and high-performance current amplifiers for *in-situ* conductivity measurements of LCCs. In 2013, the conductivity of a LCC between graphene flakes (Fig. 10a) was experimentally measured, and the LCC remained stable for a few seconds. At a constant bias voltage, the current flows through the carbon chain, and changes in monitored current were recorded. An asymmetric shape of current-voltage curve of the LCC was observed (Fig. 10b). Although the conductivity of the LCC was observed experimentally, it was much lower than that predicted for the ideal state due to localized strains and contact with the electrodes [68]. The properties of carbyne under strain were calculated based on first-principles calculations. When the LCC is stretched, Peierls transition from the cumulenic structure to the polyynic structure is predicted [111]. Experimentally, it was shown that the unstrained carbon chains were metallic cumulene, while the strained chains exhibited semiconducting polyyne (Fig. 10c). In the presence of strain, the conductivity decreased with increasing chain length, eventually leading to band gap opening [112], which confirmed the prediction that strain induction causes the metal-semiconductor transition in carbyne [111,112].

4.1.2. Mechanical properties

Experimental testing on isolated LCC poses considerable challenges, resulting in a scarcity of tests based on mechanical properties. Currently, predictions regarding the mechanical strength of carbyne were predominantly derived from theoretical calculations. The intrinsic strength of a LCC was determined through *in-situ* strong-field mechanical testing using a field emission microscopy [113,114]. Strength values of 270 GPa (at 5 K) and 251 GPa (at 77 K) were extracted experimentally, surpassing the strength of graphene (130 GPa) [114,115]. Despite limitations in the mechanical strength of LCCs based on experimental measurements, anomalous strengths exceeding that of other carbon materials are still exhibited.

The mechanical responses of carbyne to tension, bending, and torsion deformations were investigated through first-principles calculations [116]. Under tension, carbyne demonstrated a stiffness approximately twice that of the stiffest known materials and an unparalleled specific strength of up to 7.5×10^7 N m/kg, *i.e.*, requiring a force of ~10 nN to break a single atomic chain. The fracture force under tensile strain ranged between 9.3 nN and 11.7 nN at critical strains of 9%-19%. Furthermore, mechanical models were constructed to predict the mechanical strength of carbyne inside a SWCNT [117]. As the mass ratio of carbyne carbons to sheath carbons increases, the gravimetric modulus and strength of carbyne chains@SWCNT were predicted to rise from 356.4 and 50.25 to 977.2 and 71.20 GPa g^{-1} cm^3, respectively, which surpassed those of graphene or SWCNTs by 174.2% and 41.7%, respectively.

4.1.3. Optical properties

4.1.3.1. Absorption. Ultraviolet–visible (UV-vis) spectroscopy is frequently employed to characterize polyynes, where the HOMO→LUMO gap is contingent on the $\pi \rightarrow \pi^*$ transition of C≡C bonds [118]. The absorption spectra for Tr*-terminated polyynes (with varying carbon atom counts, n = 4-22) in hexanes were examined, revealing a pronounced redshift in the λ_{max} value with an increase in the number of carbon atoms (Fig. 11a). Similarly, the absorption spectra of hydrogen-capped polyyne in decahydronaphthalene showed comparable redshifts as the number of carbon atoms increased (Fig. 11b). Absorption spectra of these

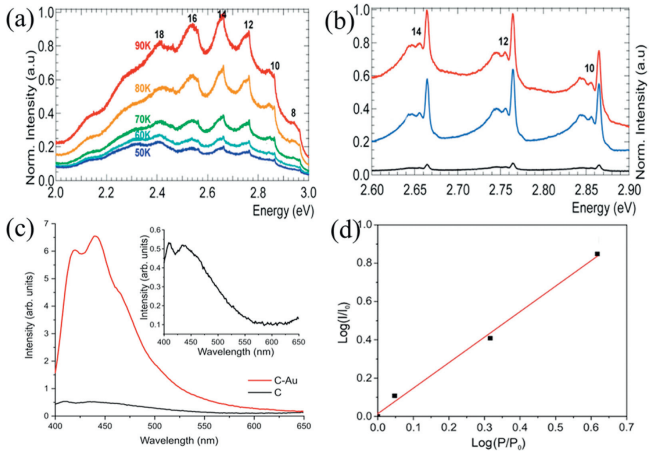

Fig. 12. (a) PL spectra of the Au-capped polyynes with different lengths at temperatures from 90 K to 50 K. (b) PL spectra of Au-capped polyynes taken at 4 K excited at 390 (Red), 380 (blue), and 370 nm (black) [125]. Copyright 2020 American Chemical Society. (c) PL spectra of H-capped polyyne (gray line) and Au-capped polyyne (red line). (d) Double logarithm plot of the integral PL intensity on the excitation power [127]. Copyright 2024, American Physical Society.

polyynes, synthesized through chemical methods, arc discharge, or laser burning techniques, are also influenced by the end-group effect [119]. Experimentally this effect diminishes as the chain lengthens, with the absorption spectrum's peak position tending to saturate at a certain wavelength [11]. Consequently, for polyynes with end-groups, the characteristic properties of carbyne can be elucidated by assessing whether spectral data converge toward a constant value (saturation) concerning chain length (Fig. 11c). In the case of LCC@CNTs, the feeble absorption characteristics of the LCCs were obscured by the robust absorption of the CNTs, making it challenging to discern contributions from the LCCs [75,105,120].

4.1.3.2. Photoluminescence. The photoluminescence (PL) of end-capped polyyne typically exhibits low efficiency [121]. Laser-induced dispersed PL spectra of polyynes, *i.e.*, $C_{2n}H_2$ ($n = 4$-9), were examined [122]. With an increase in the number of carbon atoms, the chain elongates, resulting in a redshift of the peak position. Recorded PL and excitation spectra of the Tr*[n] series in hexane solution highlight that the PL spectra mirrored the λ_{main} bands in the absorption spectra, with corresponding excitation spectra being well matches [123]. In addition, strong PL can be emanated from small crystal made from polyyne [57]. It was found that the hexagonally structured crystals luminesced from ultraviolet to near-infrared range [124], originating to the energy gap regulated by the length of the polyynes. Kutrovskaya *et al.* studied the PL of Au end-capped polyynes (contain 8 to 24 carbon atoms) [125]. The PL spectra reveal characteristic triplet fine structures of the polyynes (Fig. 12a). PL peaks of the polyynes with different lengths always consist of a sharp strong peak and two broader satellite peaks (Fig. 12b). These resonances were interpreted to be associated with the emission of edge-state neutral, positively charged and negatively charged excitons, respectively. The triple fine structure was more prominent at helium temperatures and was independent of the length of the polyynes [125]. In addition, it was shown that the primary photoinduced event is an ultrafast internal conversion (~200 fs decay time) from the bright dipole-allowed high-energy singlet state to a dark low-energy singlet state, which is not affected by the end groups capping the polyyne [126].

The enhanced PL intensity of polyynes can be observed in metal end-capped polyyne. The Au-capped polyynes exhibited significantly higher luminescence intensity compared to that of the H-capped polyynes (Fig. 12c). The presence of Au served as a source of electron doping, resulting in a linear relationship between PL intensity and excitation power (Fig. 12d) [127].

4.1.3.3. Raman spectroscopy. Raman spectroscopy serves as a distinctive fingerprint spectrum, elucidating the inelastic scattering of light by molecular vibrations or phonons [128,129]. The identification of substances can be accomplished by scrutinizing the vibrational frequencies of the substances [130].

Raman spectra of LCCs can be roughly divided into two groups: one is the Raman spectra of polyynes with different end-groups, which are usually preserved in liquid; the other is the Raman spectra of LCCs existing inside CNTs, and the CNTs as host can effectively protect the internal LCCs and maintain their stability [14]. In both cases, carbon-chain band (CC-band) is used for the definition of their Raman modes.

The H-capped polyynes obtained by arc-discharge technique was subjected to Raman spectroscopy to realize the determination of the chain length. Raman spectra in Fig. 13a suggested that the stability of H-capped polyynes was limited, because they were prone to cross-linking reactions [131]. The degree of π-electron conjugation increases with the length of the polyyne and is related to the specific termination [132]. In principle, a larger end group than hydrogen, such as phenyl or a larger end group [68], enhances the stability of the polyynes.

Phenyl-capped polyynes (Ph-Cn-Ph) up to 12 carbon atoms remained stable even when the solvent was completely removed to form a solid state (Fig. 13b) [133]. Since the excitation laser energy usually in the visible range does not match the band gap of polyynes, direct observation of Raman signal of polyynes is difficult. Therefore, surface-enhanced Raman spectroscopy (SERS) is usually applied for testing. The Raman signals of polyynes in SERS are normally red-shifted by a few wavenumbers compared with the signal obtained by normal Raman spectroscopy [91].

As mentioned above, the larger the end group, the better the stability of the polyyne. The end groups on both sides of the polyyne can be different [100,134]. The vibrational properties of a series of symmetric (SP[N]) and asymmetric (UP[N]) end-capped polyyne were investigated (Fig. 13c). Raman frequencies shifted for the chain with same length but different symmetry, because the asymmetric structure induces an electronic polarization of the chain, and this polarization effect decreases with increasing chain length [100]. In addition, it was reported that by designing polyyne with different end groups or isotope doping, different Raman frequencies can be obtained for optical imaging [135].

Electropositive transition-metal end groups can enhance the stability of the polyynes, as evidenced in the synthesis of from $PtC_{20}Pt$ to $PtC_{52}Pt$ (Fig. 13d). The Raman frequency of the PtCnPt droped from 1928 cm^{-1} ($n = 20$) to 1880 cm^{-1} ($n = 52$), and almost converged towards saturation Fig. 13e) [12]. As chain length increases the end group effect weakens, the lower the Raman frequency, because the BLA decreases as the length of the polyyne increases until the BLA saturates [91]. In addition, the Raman frequencies of the polyynes in different solvents exhibit shifts by a few wavemumbers [136].

Raman frequencies of polyynes are usually located at over 2000 cm^{-1}, and the Raman modes of the LCCs inside CNTs are at lower frequencies, usually between 1700 cm^{-1} and 1900 cm^{-1} [73], because the encapsulated LCCs are usually longer than the polyynes and the interaction between the LCC and CNTs further shifts down the Raman frequency [137].

For easy comparison, Raman frequencies of LCCs in different environments as a function of the inverse number of carbon atoms is summarized in Fig. 14a. In general, the Raman frequency tends to be proportional to the inverse of the number of carbon atoms [100,137]. In addition, a clear environmental effect can be observed, where the CNTs shift down the signal the most.

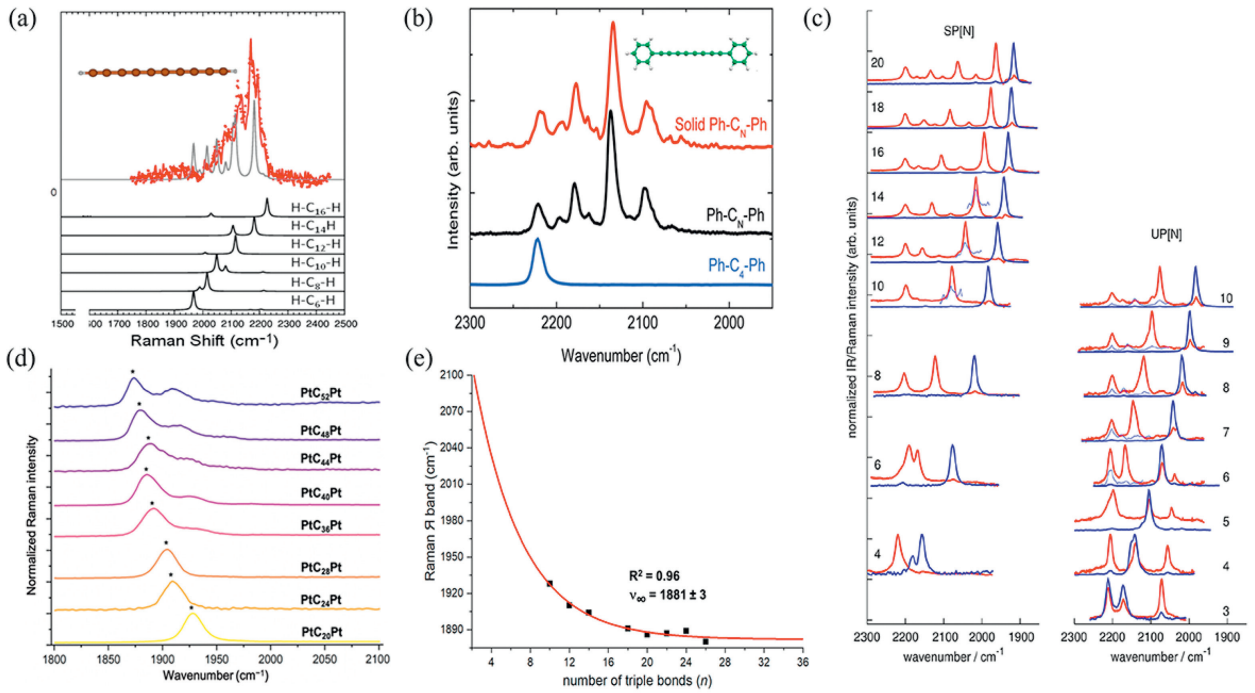

Fig. 13. (a) FT-Raman spectrum of H-capped polyynes obtained by subtraction of the methanol signal and DFT-computed Raman peaks [131]. Copyright 2006 Elsevier. (b) Raman spectra taken at 1064 nm excitation wavelength of diphenylpolyynes of different chain lengths in decalin solution, the same sample after solvent evaporation (labeled as solid Ph-C_n-Ph), and Ph-C_4-Ph diphenylpolyyne sample in solution [133]. Copyright 2011, American Chemical Society. (c) IR (red line) and Raman (blue line) spectra recorded for SP[N] (left) and UP[N] (right) in toluene solution [100] Copyright 2013 John Wiley & Sons, Ltd. (d) Raman spectra of PtC_xPt (~1 mmol/L solution in CH_2Cl_2, Я band denoted by*). (e) Extrapolation of the Raman Я band of PtC_xPt to x =∞ by using the Meier equation [12]. Copyright 2023 American Chemical Society.

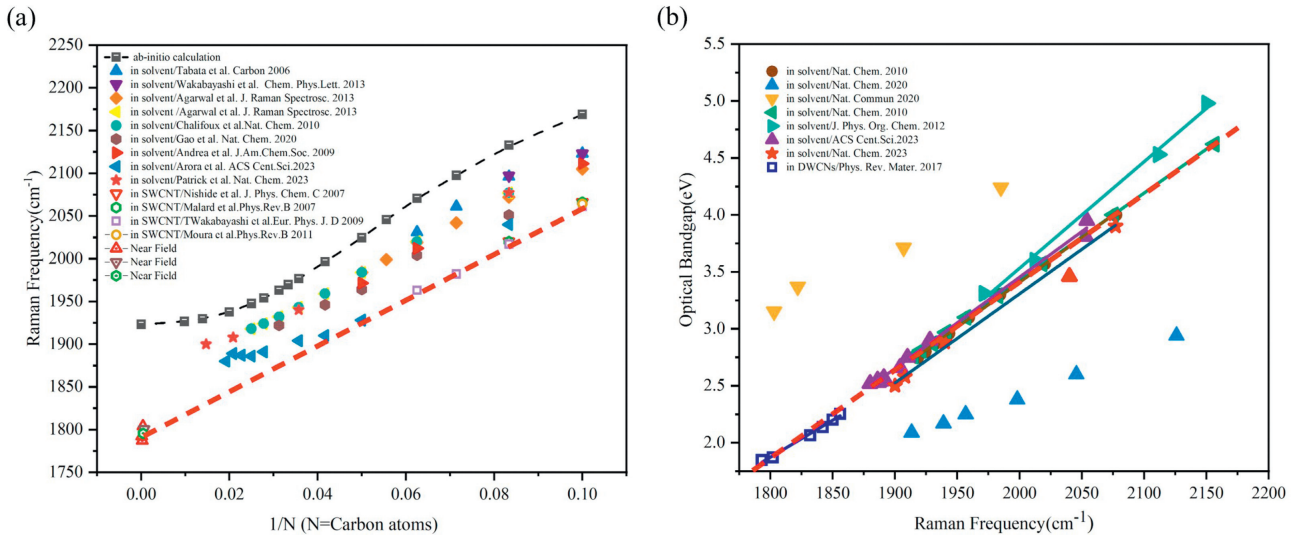

Fig. 14. (a) Raman frequencies of carbon chains in different environments as a function of the inverse number of carbon atoms. (b) Optical energy gap as a function of Raman frequency for the polyynes and LCCs in different environment.

Since both the PL and absorption of the LCCs cannot be resolved due to the existence of the CNTs, resonance Raman spectroscopy emerges as an effective method to characterize the optical band gap of the LCCs encapsulated in CNTs. The measurements of the encapsulated LCCs were performed using tunable lasers. When the laser energy matches the optical band gap of a LCC, the Raman spectrum reaches its maximum [95]. When we summarized the optical band gaps of both the polyynes obtained from absorption and the optical band gaps of the LCCs from resonance Raman spectroscopy, as summarized in Fig. 14b, a linear relationship between the optical band gap and the Raman frequency was found using the extracted data in different literatures, which is reasonable, since both the optical band gap and the Raman frequency of the carbon chain eventually depend on the BLA [95,138]. Most of the data points fall on the linear line except two sets of the data for some polyynes in solvents. How to extracting the optical band gaps of the polyynes from the absorption is an open question, because either the lowest yet extremely weak absorption component or the first pronounced component should be used for determination of the optical band gap [123].

Comparing the Raman intensity of the LCC and the intensity of graphene, it was found that LCC has the largest Raman cross section [139]. Therefore, it is able to realize anti-Stokes spectroscopy at the single-chain level. Furthermore, it was found that the evo-

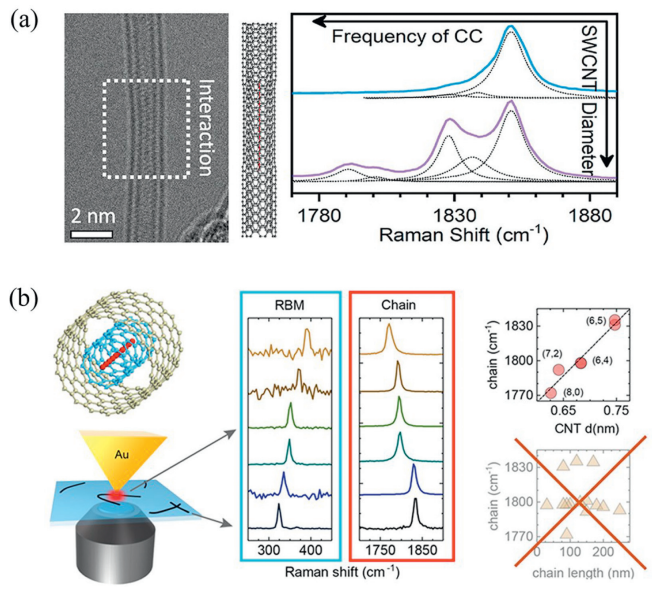

Fig. 15. (a) A TEM image of a carbon chain inside an interaction-introduced diameter-changed nanotube and the Raman spectra of the LCCs synthesized inside the CNTs with different diameters [104]. Copyright 2021, American Chemical Society. (b) TERS of several LCCs@DWCNTs and Raman spectra of the encapsulated LCCs as a function of diameter of the CNT or length of the LCCs [144]. Copyright 2018, American Chemical Society.

lution of the anti-Stokes/Stokes ratio with laser power can be well captured by a Boltzmann factor with a power-dependent equilibrium temperature [140]. Thus, the LCCs hold great promise for nanoscale anti-Stokes Raman temperature measurements.

4.1.4. Tuning properties of LCCs through CNT encapsulation

Encapsulation of LCCs inside CNTs has proven to be an effective strategy for preserving the LCCs. CNTs serve to shield the chains from external interactions, fostering efficient chain elongation. The achievement of the longest recorded LCC preparation has been attributed to the encapsulation of the CNT [14]. However, the intricate interplay between the chains and the nanotube hosts necessitates careful consideration, as it significantly influences the vibrational and electronic properties of the LCCs [141].

Theoretical calculations have played a pivotal role in predicting and understanding the interactions in such confined LCC systems. First-principles calculations were employed to investigate infinite LCCs encapsulated inside SWCNTs, revealing that the combined effects of hybridization and charge transfer result in a partial inhibition of the BLA [142]. In addition, DFT was applied to investigate the relaxation structure and electronic properties of LCC systems inside two chiral SWCNTs. It was shown that metallic conductance of the LCC@SWCNT system came from charge transfer from CNTs to the LCC [143]. Notably, experimental studies emphasized the critical role of the nanotube diameter, showcasing that it outweighs the impact of metallicity, highlighting the influence of confined LCCs on the radial shrinkage of the CNTs' cross-section and the subsequent adjustment of the band gap of LCCs by controlling the CNT diameter (Fig. 15a) [104].

Tip-enhanced Raman spectroscopy was employed to examine the isolated pairs of inner tubes of DWCNTs and encapsulated LCCs (Fig. 15b). The results indicated that the Raman frequency of the LCC was determined by the chirality of the inner tube, with a reduction in frequency observed as the inner tube's diameter decreases. Notably, there was no length dependence observed in the Raman mode frequencies of the chains, revealing that the LCCs are indeed carbyne [144]. In addition, charge transfer between the inner tube and the chains leads to a substantial up to threefold increase in the PL signal of the inner tubes with encapsulation of the LCCs compared to empty ones [105].

4.1.5. Pressure-tailored properties

Pressure-induced changes in the properties of LCCs encapsulated inside CNTs have been investigated. Their Raman frequencies exhibit anomalous behavior under pressure, appearing to decrease with increasing pressure. Two main explanations for this phenomenon have been proposed: the softening of a carbon bond under pressure or charge transfer to the chain [145,146]. Experimental and theoretical tools were employed to explore the behavior of LCCs encapsulated in the innermost shells of MWCNTs under high pressure (0-9 GPa) [147]. Unlike the G band frequencies of carbon nanotubes, which increase with pressure, the Raman frequencies of the LCCs were observed to decrease (Fig. 16a).

Two main explanations for this phenomenon have been proposed: the softening of the carbon-carbon bonds under pressure or charge transfer from the CNTs to the LCCs [145,146]. The pressure-induced irreversible structural changes in LCCs were interpreted as the coalescence of the LCCs [147]. As shown in Fig. 16b, resonance Raman spectroscopy on LCCs@DWCNT indicated a non-linear decrease in the frequency of the CC-band as pressure increased. This was attributed to a significant increase in charge transfer from the tube to the chain induced by pressure. Tube-chain cross-linking occurred near the collapse pressure of the tubes [146]. A separate investigation into the structural transitions and band-gap evolution of LCCs encapsulated in DWCNTs under high pressure revealed that a band gap linearly decreased by up to 0.2 eV with increasing pressure from 0 to 51 GPa (Fig. 16c) [148].

Except electrical properties, mechanical properties of LCCs can also be extracted from the pressure-induced changes in Raman spectra of LCCs inside MWCNTs. The triple bond and the single bond both deform when the LCCs were subjected to external pressure, but the single bond contributed more to the frequency change [149]. The relationship between the strain and pressure (P) was explained by considering the natural incongruity of single bond [150]. A straightforward anharmonic force-constant model reveals that the Young's modulus (E) and Grüneisen parameter (γ) follow universal laws of P^{-1} and the strain (ε) of the LCCs follows a P^2 law (Figs. 17a-d) [145].

4.2. Properties of cyclo[n]carbon

The aromaticity and physical properties of fully conjugated planar carbon rings are of significant interest in current research on cyclic carbons. As research in this area has advanced, we provide a concise overview of these properties from two perspectives.

4.2.1. Aromaticity

Aromaticity, considered an intrinsic property of molecules, is closely associated with electron delocalization, stability, and other characteristics. Shocker's rule [151] is commonly employed to determine aromaticity, stating that a cyclo[n=4m+2]carbon (where m is a positive integer) is energetically stable due to the accommodation of all (4m+2) π-electrons in its bonding molecular orbitals. In contrast, cyclo[n=4m]carbon was predicted to be less stable and display double anti-aromaticity [9,152]. Thus, cyclo[n]carbon is characterized as double aromaticity if both π_{in} and π_{out} contain 4m+2 electrons, and double antiaromaticity character if both π_{in} and π_{out} contain 4m electrons. In addition, it can also be a mixture of π_{in} aromaticity and π_{out} anti-aromaticity. Another way to quantify the aromaticity of a cyclo[n]carbon is to observe how the ring carbon behaves in the presence of an external magnetic field [153,154]. It can usually be analyzed from the following perspective: anisotropy of current-induced density, the gauge-including

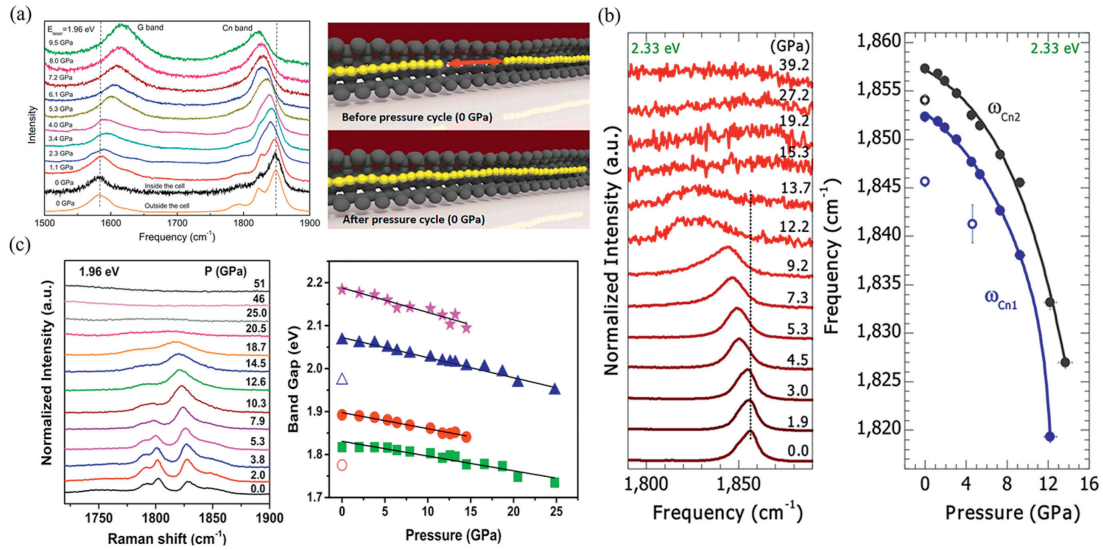

Fig. 16. (a) Raman spectra of LCCs@MWCNTs under pressure (0-9 GPa) and diagrams of LCC coalescence [146]. Copyright 2015, American Chemical Society. (b) Raman spectra of LCCs@DWCNTs under pressure (0.0-39.2 GPa) and Raman frequency as a function of pressure [146]. Copyright 2018 Elsevier Ltd. (c) Raman spectra of LCCs@DWCNTs under pressure (0-51 GPa) and band gap of the LCCs as a function of pressure during compression (solid symbols) and decompression (empty symbols) [148]. Copyright 2019 Elsevier Ltd.

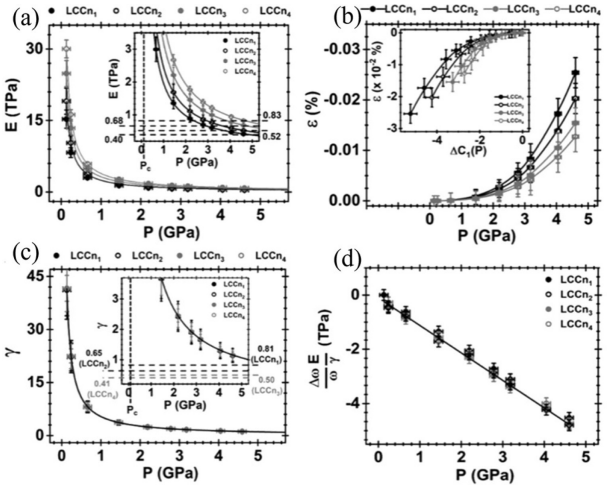

Fig. 17. Mechanical parameters as a function of *P*: (a) Young's modulus (*E*), (b) strain (ε), and (c) Grüneisen parameter (γ), and (d) $\Delta\omega E/\omega\gamma = -P$, as a function *P* [145]. Copyright 2020 American Physical Society.

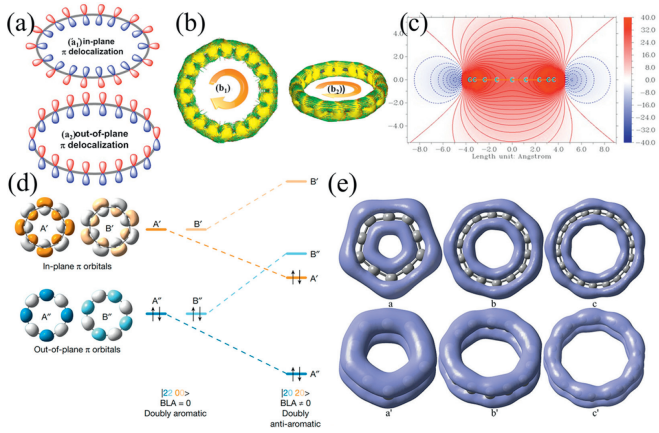

Fig. 18. (a) Two sets of π electron delocalizations in the cyclo[18]carbon. (b) Isosurface maps of the anisotropy in the current-induced density of the cyclo[18]carbon formed by π_{in} electrons or π_{out} electrons. (c) Contour map of the iso-chemical shielding surface of the cyclo[18]carbon in the slice plane perpendicular to the ring [153]. Copyright 2020, Elsevier Ltd. (d) Frontier orbitals of two electronic states of cyclo[16]carbon [17]. Copyright 2023, Nature. (e) Localized molecular orbitals for cyclo[10]carbon (a, a'), cyclo[14]carbon (b, b') and cyclo[18]carbon (c, c') [160]. Copyright 2020, Royal Society of Chemistry.

magnetically induced current and Iso-chemical shielding surface [153]. The other technique to quantify the degree of aromaticity is the BLA in cyclo[*n*]carbons [155-157].

The unique "double" aromaticity of cyclo[18]carbon arises from the delocalization of two scaffolds of 18 π-electrons oriented both in the plane of the ring and perpendicular to it [84]. DFT calculations and complete active space-self-consistent field levels confirmed that polyynic structure is the global minimum for the cyclo[18]carbon, aligning with experimental observations [18,158]. Meanwhile, application of a magnetic field to cyclo[18]carbon showed strongly anisotropic ring currents, confirming its aromaticity, which is consistent with the Hückel rule (Fig. 18b). Analysis of the induced magnetic field in cyclo[*n*]carbon rings ($n = 6$-28) suggested that cyclo[n=4m+2]carbon and cyclo[n=4m]carbon possessed dual aromatic and antiaromatic properties, respectively [159]. An exploration of the thermodynamic stabilities of cyclo[*n*]carbon ($4 \le n \le 34$) using hybrid DFT indicated that cyclo[*n*]carbon ($10 \le n \le 34$, $n = 4m + 2$) would be thermodynamically stable. Notably, cyclo[n=8, 10, 14]carbon exhibited substantial aromaticity attributed to two perpendicular delocalized π orbitals, encompassing both π_{out} and π_{in} [160].

Recently, experimental observations revealed that cyclo[10]carbon and cyclo[14]carbon exhibit cumulenic structure, whereas cyclo[16]carbon and cyclo[18]carbons feature polyynic structure [16-18]. Cyclo[n=10, 14, 18]carbons conform to the Hückel (4m+2) rule, rendering them doubly aromatic. Cyclo[n=16]carbon conforms to the Hückel (4m) rule, suggesting that it has doubly aromatic. A recent study confirmed its dual antiaromaticity by observing the BLA of the cyclo[16]carbon [17].

Typically, antiaromatic molecules are less stable compared to their aromatic counterparts. A study achieved a complete reversal of the antiaromatic character in cyclo[16]carbon by introducing metal atoms into the ring, facilitating electron transfer between cyclo[16]carbon and the encapsulated metal atoms to induce

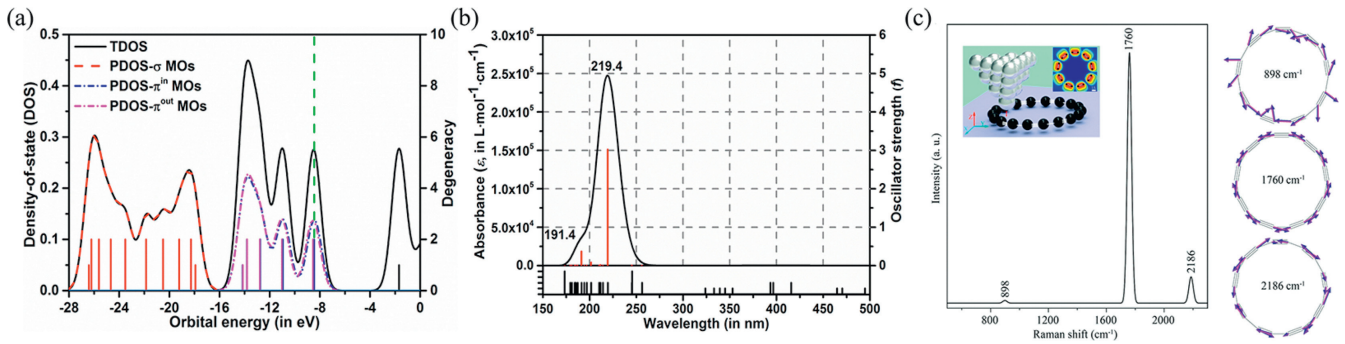

Fig. 19. (a) Density-of-state map (curve) and molecular orbitals degeneracy (spikes) of the cyclo[18]carbon. The location of the HOMO is highlighted by a green dashed line. (b) Simulated UV-vis absorption spectrum (curve) and oscillator strength (red spikes) of the cyclo[18]carbon [162]. Copyright 2020, Elsevier Ltd. (c) The calculated normal Raman spectrum and the vibrational modes of cyclo[18]carbon [165]. Copyright 2020, Royal Society of Chemistry.

aromaticity [161]. Another investigation reversed the antiaromatic properties of cyclo[16]carbon by controlling the BLA. This manipulation caused an abrupt reversal of the induced cyclo[16]carbon ring current, achieving aromaticity with only a minimal change in energy and without significant alterations in the electronic structure [156].

4.2.2. Calculated properties

Physical property of cyclo[*n*]carbon molecules have not been experimentally determined, but theoretical calculations have made certain predictions, which would help to advance the experiment. Geometry optimization and excitation energy calculation of the cyclo[18]carbon were realized by DFT and time-dependent DFT (TD-DFT). The HOMO-LUMO gap for cyclo[18]carbon was calculated as 6.75 eV (Fig. 19a) [162]. Additionally, the absorption spectrum of cyclo[18]carbon was computed, revealing an intense absorption band originating from doubly degenerate excitations (S0 → S21 and S0 → S22), with a UV-vis absorption maximum at 219.4 nm (Fig. 19b). This result is almost the same as the absorption peak calculated by TD-DFT [163]. In contrast, static HOMO-LUMO gap of cyclo[18]carbon was calculated by Hybrid DFT calculations on a B3LYP/6-311G (d,p) level to be 3.1 eV, while TD-DFT at the same level indicated an optical band gap of 2.44 eV [164].

Besides, the Raman spectrum of cyclo[18]carbon was uncovered through quantum chemical calculations. Strong bands at 1760 and 2186 cm^{-1} were attributed to C≡C symmetric and antisymmetric stretching, respectively, while a weak band at 898 cm^{-1} corresponds to C-C stretching mixed with bending vibrations (Fig. 19c) [165].

5. Applications of carbon chains

The unique sp hybrid structure of the carbon chains gives them excellent properties. Theory predicts that sp^1-hybridized carbon chains with very high mechanical strength are expected to be used for mechanical reinforcement and aerospace materials [116,166]. The tunable optical band gaps of carbon chains are typical semiconductors, which make them promising for the preparation of single-atom-width transistors. In addition, the optical properties of carbon chains reveal that they can be used in the field of light-emitting materials. Although fundamental researches on the sp^1-hybridized materials are still ongoing, their excellent properties have already been highlighted in applications.

The most basic component used to fabricate functional devices is the molecular wire. It typically requires a rigid linear molecular backbone and a π-conjugated electronic structure that can facilitate electron transport [167]. The simplest π-conjugated organic molecules are linear sp^1-hybridized carbon structures, which enable the electron density to create a nearly cylindrical distribu-

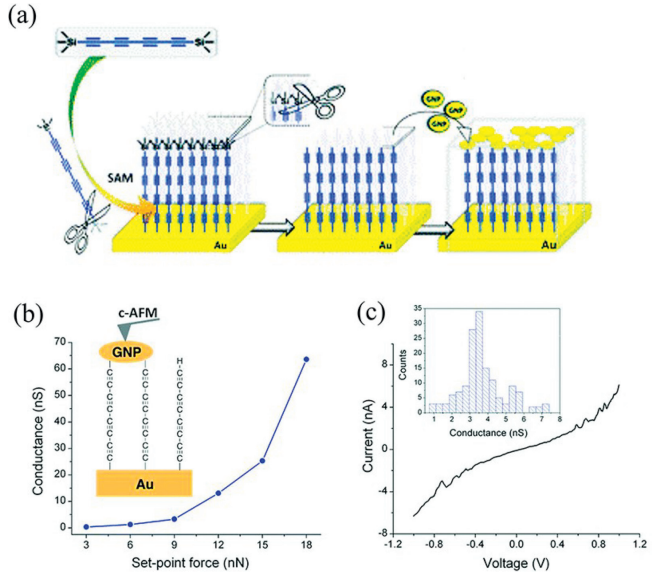

Fig. 20. (a) Schematic diagram for preparation of Au|C_8|GNP, a nascent metal monolayer metal device characterised by "all-carbon" molecular wires. (b) The measurement of average conductance. (c) Representative *I–V* curve experimentally obtained by positioning the c-AFM tip on top of GNP when a set-point force of 9 nN was applied [170]. Copyright 2018, Royal Society of Chemistry.

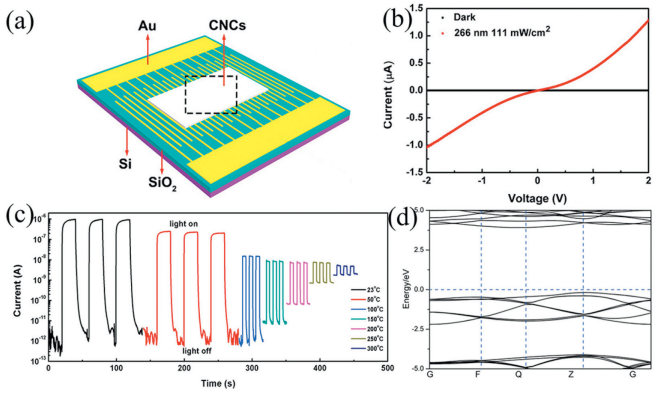

Fig. 21. (a) The 3D schematic diagrams of the photodetector using polyyne nanocrystals. (b) *I–V* curves ofthe device under dark and irradiation at 266 nm light. (c) On/off switching characterization of the device with temperatures ranged from 25 °C to 300 °C, measured at a bias of 2 V under the illumination of 266 nm ligh. (d) Band structure of the polyyne nanocrystals by the first-principles calculations [171]. Copyright 2021, Wiley-VCH GmbH.

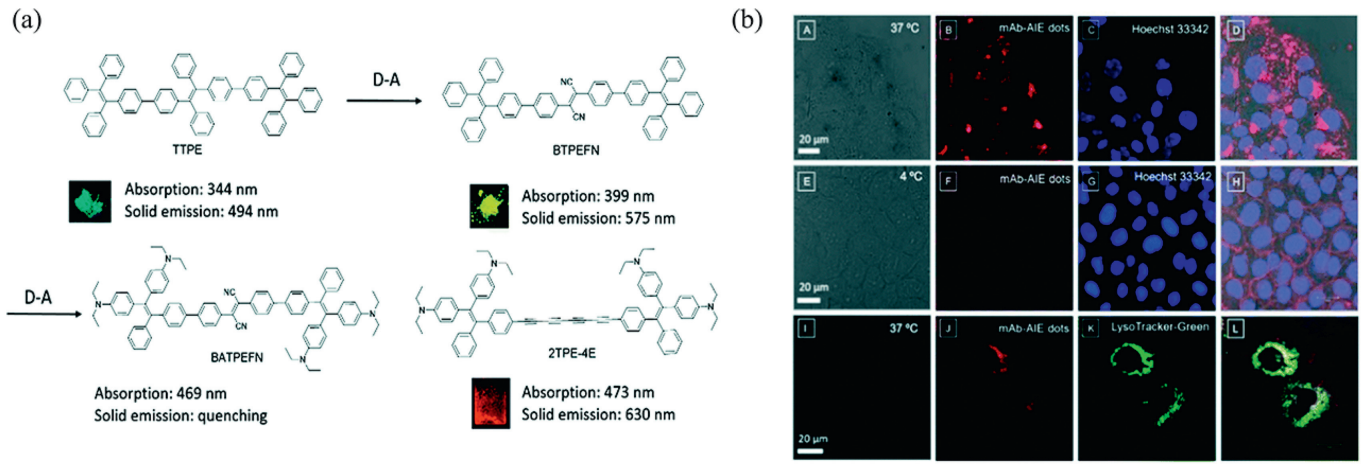

Fig. 22. (a) The preparation strategies of a molecule based on a polyyne. (b) Specific recognition of mAb-AIE probes and cell imaging images [175]. Copyright 2017, Royal Society of Chemistry.

tion along a one-dimensional, rigid, and length-persistent backbone [168,169]. Based on this, a novel molecular electronic device (metal–monolayer-metal devices with "all-carbon" molecular bridges) has been developed (Fig. 20a) [170]. Analysis of the *I-V* curve excludes the presence of a short circuit and shows that 9 nN was the minimum set point force required for a reasonable contact between the tip and the gold nanoparticles (GNP) (Figs. 20b and c). The molecular wires Au|C_8|GNP showed encouragingly high conductivity through testing.

A high-performance photodetector made of polyyne nanocrystals with a wide bandgap was reported (Fig. 21a) [171]. As shown in Fig. 21b, the current of this detector was significantly affected by the biased piezoelectric voltages when it was illuminated by light. The light response of this sensor at different temperatures shown in Fig. 21c suggested that the device maintained a good signal-to-noise ratio and faster response recovery at conditions up to 300 °C. Calculations showed that the electron mobility of a single carbon chain was comparable to that of graphene, and the good transport properties of a single carbon chain ensured the high performance of the device [172]. The calculated bandgap of the CNC was 4.1 eV (Fig. 21d), suggesting that it is a typical semiconductor. There was a thin electron depletion layer on the surface of the device, which created a high barrier height, and generated very few electron-hole pairs in the dark, thus producing a high sensor resistance. When exposed to light, the polyyne nanocrystals produced electron-hole pairs. In this case, the electron depletion layer was thinner and the barrier height decreased [172]. Based on this mechanism, a visible-light-driven room-temperature gas sensor prepared with the polyyne nanocrystals was created. This sensor allows to detect NO_2 in gas at concentration of as low as 2 ppm, and has good sensing effect and stability [173].

LCCs and metal nanoparticles embedded in a porous matrix of titanium dioxide nanotubes enable strong resonance absorption on complex hypersurfaces in the visible range by adjusting the diameter of the nanotubes and the concentration of the metal nanoparticles. The LCC clusters embedded in transparent titanium dioxide tubes act as atomic wires, and the highly efficient conductivity of the sp^1-hybridized carbon chains in combination with the enhanced absorption of light by the plasma enabled the preparation of periodic photosensitive photodiode [174].

Polyyne has a special conjugated structure, and increasing the π-conjugation of organic π-segments by linking them together can give the resulting materials unique optoelectronic and physical properties [102]. A novel polyyne-bridged aggregation-induced emission (AIE) luminogen with red light emission was prepared. As shown in Fig. 22a, two diethylamine-substituted tetraphenylethylene (TPE) were connected by a polyyne to prepare the luminant molecule with long wavelength absorption and red emission. Polyyne not only acts as a bridge to expand π-conjugation, but also as an electron acceptor, which promotes intramolecular charge transfer and enhances the stability of luminescence. It was successfully used for targeted imaging of cancer cells and monitoring of receptor-mediated endocytosis process (Fig. 22b) [175]. Since the Raman frequency of the polyyne shifts to lower frequencies with increasing length. By rationally designing the conjugation length, bond-selective isotope labeling and end-capping substitution of polyyne, 20 different Raman frequencies can be realized. The researchers achieved frequency tuning in the range of 20-80 cm^{-1} by selective labelling of polyyne with ^{13}C bonds. In combination with different end-cap substitutions for fine-tuning the frequency of the polymer, a ten-colour organelle imaging technique was developed for biological living cells, which can display multiple species simultaneously. In addition, this broad spectrum of polymers (carbow) can be used for optical data storage and identification. Using polymer beads as information carriers, spectral barcodes with ten recognisable frequencies can be realised at three different intensities. Compared to previous optical barcode materials, it provides more recognizable frequencies without the complexity of photobleaching or energy transfer [135].

For comparison, cumulene has less stability compared to polyyne, and the longest cumulene consists of only 9 consecutive double bonds [33]. A first field-effect transistor employing tetraphenyl[3]cumulene was fabricated by solution drop casting [176]. Subsequently, an improved meniscus-coating technique allows to fabricate transistors with hole mobilities of greater than 0.1 $cm^2\ V^{-1}\ s^{-1}$ [177]. The [*n*]cumulenes with an odd number of double bonds are more conductive than expected for their length, which is much higher than that of [2]cumulene, because of its twisted geometry [178].

6. Conclusion and outlook

In this comprehensive review, we have succinctly outlined the synthetic methodologies and characteristics of sp^1-hybridized carbon chains, including LCCs and cyclo[*n*]carbon. The review encompasses significant milestones in trial developments and provides a thorough overview of the evolution of research on the LCCs and cyclic carbons, spanning from their initial discovery to contemporary observations. As synthetic technologies continue to advance, the enigmatic realm surrounding the carbon chains is grad-

ually dissipating, and there has been a notable transition from theoretical concepts to practical breakthroughs in the realization carbon-chain materials. Despite these strides, the persistent challenge lies in achieving controlled and scalable preparation of carbon chains, given the inherent high reactivity associated with sp^1-hybridization. Addressing this remains a prominent focus in current research endeavors. Moreover, the diverse properties exhibited by sp^1-hybridized carbon chains have been consistently validated, prompting a deeper exploration of their application potential. The ongoing quest involves harnessing these properties in innovative ways, directing research towards the development of practical applications that leverage the unique characteristics of sp^1-hybridized carbon chains.

Future research prospects primarily revolve around fundamental studies. Regarding LCCs, a significant milestone involves exploring the transition length from polyyne to carbyne, which remains an open question, although previous studies suggest a range from several to 30 nanometers. Additionally, it's crucial to experimentally determine the properties of single carbon chains. For instance, theoretical predictions indicate that the stress modulus is the highest among all materials, surpassing even that of CNTs and graphene. However, direct measurements are still lacking. Similarly, while the thermal conductivity of carbyne is predicted to be the highest among all materials, practical testing is necessary for confirmation. As for cyclo[*n*]carbon, the key question pertains to its minimum and maximum sizes and how properties vary with the size of the ring. Exploring these aspects will contribute significantly to advancing the understanding of these unique carbon structures. In summary, this review underscores both the progress made and the compelling avenues for future exploration in the dynamic field of sp^1-hybridized carbon chains.

Declaration of competing interest

The authors declare that they have no known competing financial interests or personal relationships that could have appeared to influence the work reported in this paper.

CRediT authorship contribution statement

Huiju Cao: Writing – original draft. **Lei Shi:** Writing – review & editing, Supervision, Funding acquisition, Conceptualization.

Acknowledgments

This work was supported by National Natural Science Foundation of China (No. 52472059), Fundamental Research Funds for the Central Universities, Sun Yat-sen University (No. 22lgqb03), and State Key Laboratory of Optoelectronic Materials and Technologies (No. OEMT-2022-ZRC-01).

References

[1] H.W. Kroto, J.R. Heath, S.C. O'Brien, et al., Nature 318 (1985) 162–163.
[2] S. Iijima, Nature 354 (1991) 56–58.
[3] K.S. Novoselov, A.K. Geim, S.V. Morozov, et al., Science 306 (2004) 666–669.
[4] R.B. Heimann, S.E. Evsvukov, Y. Koga, Carbon 35 (1997) 1654–1658.
[5] H.R.B. Kudryavtsev Y P, S E Evsyukov, J. Mater. Sci. 3 (1996) 5557–5571.
[6] R.B. Heimann, S. Evsyukov, L. Kavan, Carbyne and Carbynoid Structures, 1st. Ed, Kluwer Academic Publishers, Dordrecht, The Netherlands, 1999.
[7] G. Yang, Mater. Sci. Eng. R Rep. 151 (2022) 100692.
[8] K. Raghavachari, D.L. Strout, G.K. Odom, et al., Chem. Phys. Lett. 214 (1993) 357–361.
[9] J. Hutter, H.P. Luethi, F. Diederich, J. Am. Chem. Soc. 116 (1994) 750–756.
[10] W.A. Chalifoux, R.R. Tykwinski, Nat. Chem. 2 (2010) 967–971.
[11] Y. Gao, Y. Hou, F.Gordillo Gámez, et al., Nat. Chem. 12 (2020) 1143–1149.
[12] A. Arora, S.D. Baksi, N. Weisbach, et al., ACS Cent. Sci. 9 (2023) 2225–2240.
[13] C.W. Patrick, Y. Gao, P. Gupta, et al., Nat. Chem. 16 (2023) 193–200.
[14] L. Shi, P. Rohringer, K. Suenaga, et al., Nat. Mater. 15 (2016) 634–639.
[15] F. Albrecht, I. Rončević, Y. Gao, et al., Science 384 (2024) 677–682.
[16] L. Sun, W. Zheng, W. Gao, et al., Nature 623 (2023) 972–976.
[17] Y. Gao, F. Albrecht, I. Rončević, et al., Nature 623 (2023) 977–981.
[18] K. Kaiser, L.M. Scriven, F. Schulz, et al., Science 365 (2019) 1299–1301.
[19] A.G. Whittaker, Nature 276 (1978) 695–696.
[20] X. Liu, G. Zhang, Y.W. Zhang, J. Phys. Chem. C 119 (2015) 24156–24164.
[21] J. Szczepanski, J. Fuller, S. Ekern, et al., Spectrochim. Acta Part A 57 (2001) 775–786.
[22] A. Karpfen, J. Phys. C: Solid State Phys. 12 (1979) 3227.
[23] D. Wendinger, J.A. Januszewski, F. Hampel, et al., Chem. Commun. 51 (2015) 14877–14880.
[24] J.A. Januszewski, R.R. Tykwinski, Chem. Soc. Rev. 43 (2014) 3184–3203.
[25] E.C. Kenneth, S. Pitzer, J. Am. Chem. Soc. 81 (1959) 4477–4485.
[26] P. Siemsen, R.C. Livingston, F. Diederich, Angew. Chem. Int. Ed. 39 (2000) 2632–2657.
[27] A.S. Hay, J. Org. Chem. 27 (1962) 3320–3321.
[28] W.A. Chalifoux, R.R. Tykwinski, C.R. Chim. 12 (2009) 341–358.
[29] F. Bohlmann, Polyacetylenen 86 (1953) 657–667.
[30] M. Jevric, M.B. Nielsen, Asian J. Org. Chem. 4 (2015) 286–295.
[31] C.W. Patrick, J.F. Woods, P. Gawel, et al., Angew. Chem. Int. Ed. 61 (2022) e202116897.
[32] N. Weisbach, Z. Baranová, S. Gauthier, et al., Chem. Commun. 48 (2012) 7562–7564.
[33] D. Wendinger, R.R. Tykwinski, Acc. Chem. Res. 50 (2017) 1468–1479.
[34] P. Gawel, S.L. Woltering, Y. Xiong, et al., Angew. Chem. Int. Ed. 60 (2021) 5941–5947.
[35] V. Scuderi, S. Scalese, S. Bagiante, et al., Carbon 47 (2009) 2134–2137.
[36] X. Song, Y. Liu, J. Zhu, Carbon 44 (2006) 1584–1586.
[37] M. Jinno, S. Bandow, Y. Ando, Chem. Phys. Lett. 398 (2004) 256–259.
[38] Y.A. Kim, H. Muramatsu, T. Hayashi, et al., Carbon 50 (2012) 4588–4595.
[39] C.T. Kingston, B. Simard, Anal. Lett. 36 (2003) 3119–3145.
[40] F. Cataldo, Carbon 42 (2004) 129–142.
[41] F. Cataldo, Tetrahedron Lett. 45 (2004) 141–144.
[42] F. Cataldo, Polyhedron 23 (2004) 1889–1896.
[43] Y. Wu, Y. Zhang, T. Zhu, et al., Chem. Phys. Lett. 730 (2019) 64–69.
[44] H. Li, Y. Wu, Y. Zhang, et al., Chem. Phys. 535 (2020) 110804.
[45] Y.F. Zhang, Chin. Phys. B 31 (2022) 125201.
[46] X. Zhao, Y. Ando, Y. Liu, et al., Phys. Rev. Lett. 90 (2003) 187401.
[47] E. Cazzanelli, M. Castriota, L.S. Caputi, et al., Phys. Rev. B 75 (2007) 121405.
[48] N.F. Andrade, T.L. Vasconcelos, C.P. Gouvea, et al., Carbon 90 (2015) 172–180.
[49] L. Kavan, Chem. Rev. 97 (1997) 3061–3082.
[50] T.T. Masaharu Tsuji, Shingo Kuboyama, Seong-Ho Yoon, et al., Chem. Phys. Lett. 355 (2002) 101–108.
[51] R. Matsutani, T. Kakimoto, K. Wada, et al., Carbon 46 (2008) 1103–1106.
[52] R. Matsutani, F. Ozaki, R. Yamamoto, et al., Carbon 47 (2009) 1659–1663.
[53] K. Inoue, R. Matsutani, T. Sanada, et al., Carbon 48 (2010) 4209–4211.
[54] R. Matsutani, K. Inoue, T. Sanada, et al., J. Photochem. Photobiol. A 240 (2012) 1–4.
[55] P. Marabotti, S. Peggiani, A. Vidale, et al., Chin. Phys. B 31 (2022) 125202.
[56] P. Marabotti, S. Peggiani, S. Melesi, et al., Small (2024) 2403054.
[57] B. Pan, J. Xiao, J. Li, et al., Sci. Adv. 1 (2015) e1500857.
[58] P. Tarakeshwar, P.R. Buseck, H.W. Kroto, J. Phys. Chem. Lett. 7 (2016) 1675–1681.
[59] H. Kim, P. Tarakeshwar, M. Meneghetti, et al., Carbon 205 (2023) 546–551.
[60] W. Gao, C. Zhang, Z. Zhou, et al., Chin. Phys. B 31 (2022) 128101.
[61] L. Shang, F. Kang, W. Gao, et al., Nanomaterials 12 (2022) 137.
[62] Q. Sun, L. Cai, S. Wang, et al., J. Am. Chem. Soc. 138 (2016) 1106–1109.
[63] X. Yu, X. Li, H. Lin, et al., J. Am. Chem. Soc. 142 (2020) 8085–8089.
[64] W. Gao, F. Kang, X. Qiu, et al., ACS Nano 16 (2022) 6578–6584.
[65] W. Gao, L. Cai, F. Kang, et al., J. Am. Chem. Soc. 145 (2023) 6203–6209.
[66] W. Gao, W. Zheng, L. Sun, et al., Natl. Sci. Rev. 11 (2024) nwae031.
[67] C. Jin, H. Lan, L. Peng, et al., Phys. Rev. Lett. 102 (2009) 205501.
[68] O. Cretu, A.R. Botello-Mendez, I. Janowska, et al., Nano Lett. 13 (2013) 3487–3493.
[69] H.E. Troiani, M. Miki-Yoshida, G.A. Camacho-Bragado, et al., Nano Lett. 3 (2003) 751–755.
[70] R. Senga, H.P. Komsa, Z. Liu, et al., Nat. Mater. 13 (2014) 1050–1054.
[71] C. Fantini, E. Cruz, A. Jorio, et al., Phys. Rev. B 73 (2006).
[72] L. Shi, L. Sheng, L. Yu, et al., Nano Res. 4 (2011) 759–766.
[73] C. Zhao, R. Kitaura, H. Hara, et al., J. Phys. Chem. C 115 (2011) 13166–13170.
[74] J. Zhang, Y. Feng, H. Ishiwata, et al., ACS Nano 6 (2012) 8674–8683.
[75] L. Shi, K. Yanagi, K. Cao, et al., ACS Nano 12 (2018) 8477–8484.
[76] L.M. Malard, D. Nishide, L.G. Dias, et al., Phys. Rev. B 76 (2007) 233412.
[77] D. Nishide, H. Dohi, T. Wakabayashi, et al., Chem. Phys. Lett. 428 (2006) 356–360.
[78] W. Chang, F. Liu, Y. Liu, et al., Carbon 183 (2021) 571–577.
[79] K. Asaka, S. Toma, Y. Saito, SN Appl. Sci. 1 (2019) 493.
[80] H.L. Anderson, C.W. Patrick, L.M. Scriven, et al., B. Chem. Soc. Jpn. 94 (2021) 798–811.
[81] C. Lifshitz, Int. J. Mass Spectrom. 200 (2000) 423–442.
[82] W. Weltner Jr., K.R. Thompson, R.L. DeKock, J. Am. Chem. Soc. 93 (1971) 4688–4695.
[83] A.E. Boguslavskiy, J.P. Maier, Phys. Chem. Chem. Phys. 9 (2007) 127–130.
[84] F. Diederich, Y. Rubin, C.B. Knobler, et al., Science 245 (1989) 1088–1090.
[85] F. Diederich, Y. Rubin, O.L. Chapman, et al., Helv. Chim. Acta 77 (2004) 1441–1457.
[86] Y. Tobe, R. Umeda, N. Iwasa, et al., Chem. Eur. J. 9 (2003) 5549–5559.

[87] Y. Rubin, M. Kahr, C.B. Knobler, et al., J. Am. Chem. Soc. 113 (1991) 495–500.
[88] Y. Tobe, T. Fujii, H. Matsumoto, et al., J. Am. Chem. Soc. 122 (2000) 1762–1775.
[89] L.M. Scriven, K. Kaiser, F. Schulz, et al., J. Am. Chem. Soc. 142 (2020) 12921–12924.
[90] C.S. Casari, M. Tommasini, R.R. Tykwinski, et al., Nanoscale 8 (2016) 4414–4435.
[91] A. Milani, M. Tommasini, V. Russo, et al., Beilstein J. Nanotechnol. 6 (2015) 480–491.
[92] A. Milani, M. Tommasini, D. Fazzi, et al., J. Raman Spectrosc. 39 (2007) 164–168.
[93] C.S. Casari, A. Milani, MRS Commun. 8 (2018) 207–219.
[94] Y. Gao, R.R. Tykwinski, Acc. Chem. Res. 55 (2022) 3616–3630.
[95] L. Shi, P. Rohringer, M. Wanko, et al., Phys. Rev. Mater. 1 (2017) 075601.
[96] R. Hoffmann, Angew. Chem. Int. Ed. 26 (1987) 846–878.
[97] M. Kertesz, S. Yang, Phys. Chem. Chem. Phys. 11 (2009) 425–430.
[98] E. Mostaani, B. Monserrat, N.D. Drummond, et al., Phys. Chem. Chem. Phys. 18 (2016) 14810–14821.
[99] G. Onida, N. Manini, L. Ravagnan, et al., Phys. Status Solidi B 247 (2010) 2017–2021.
[100] N.R. Agarwal, A. Lucotti, D. Fazzi, et al., J. Raman Spectrosc. 44 (2013) 1398–1410.
[101] C.D. Zeinalipour-Yazdi, D.P. Pullman, J. Phys. Chem. B 112 (2008) 7377–7386.
[102] A.D.S. Sara Eisler, Erin Elliott, Thanh Luu, et al., J. Am. Chem. Soc. 127 (2005) 2666–2676.
[103] M.R. Bryce, J. Mater. Chem. C 9 (2021) 10524–10546.
[104] L. Shi, R. Senga, K. Suenaga, et al., Nano Lett. 21 (2021) 1096–1101.
[105] P. Rohringer, L. Shi, P. Ayala, et al., Adv. Funct. Mater. 26 (2016) 4874–4881.
[106] R. Liu, H. Liu, Y. Li, et al., Nanoscale 6 (2014) 11336–11343.
[107] P. Ayala, R. Arenal, M. Rümmeli, et al., Carbon 48 (2010) 575–586.
[108] K. Zhang, J. Li, P. Liu, et al., Chin. Phys. B 31 (2022) 123102.
[109] E.R. Mucciolo, A.H. Castro Neto, C.H. Lewenkopf, Phys. Rev. B 79 (2009) 075407.
[110] Y. Wu, P.A. Childs, Nanoscale Res. Lett. 6 (2010) 62.
[111] V.I. Artyukhov, M. Liu, B.I. Yakobson, Nano Lett. 14 (2014) 4224–4229.
[112] A. La Torre, A. Botello-Mendez, W. Baaziz, et al., Nat. Commun. 6 (2015) 6636.
[113] I.M. Mikhailovskij, E.V. Sadanov, S. Kotrechko, et al., Phys. Rev. B 87 (2013) 045410.
[114] S. Kotrechko, I. Mikhailovskij, T. Mazilova, et al., Nanoscale Res. Lett. 10 (2015) 24.
[115] C. Lee, X. Wei, J.W. Kysar, et al., Science 321 (2008) 385–388.
[116] M. Liu, V.I. Artyukhov, H. Lee, et al., ACS Nano 7 (2013) 10075–10082.
[117] E. Gao, R. Li, R.H. Baughman, ACS Nano 14 (2020) 17071–17079.
[118] G. Schermann, F.Hampel T.Grösser, et al., Chem. Eur. J. 3 (1997) 1105–1112.
[119] T. Gibtner, F. Hampel, J.P. Gisselbrecht, et al., Chem. Eur. J. 8 (2002) 408–432.
[120] P. Rohringer, L. Shi, X. Liu, et al., Carbon 74 (2014) 282–290.
[121] S.C. Shim, Chem. Commun. 23 (1996) 2609–2614.
[122] T. Wakabayashi, H. Nagayama, K. Daigoku, et al., Chem. Phys. Lett. 446 (2007) 65–70.
[123] J. Zirzlmeier, S. Schrettl, J.C. Brauer, et al., Nat. Commun. 11 (2020) 4797.
[124] J. Xiao, J. Li, G. Yang, Small 13 (2017) 1603495.
[125] S. Kutrovskaya, A. Osipov, S. Baryshev, et al., Nano Lett. 20 (2020) 6502–6509.
[126] P. Kabaciński, P. Marabotti, D. Fazzi, et al., J. Am. Chem. Soc. 145 (2023) 18382–18390.
[127] A. Kucherik, A. Osipov, V. Samyshkin, et al., Phys. Rev. Lett. 132 (2024) 056902.
[128] E.B. Barros, H. Son, G.G. Samsonidze, et al., Phys. Rev. B 76 (2007) 045425.
[129] M.A. Pimenta, A. Marucci, S.A. Empedocles, et al., Phys. Rev. B 58 (1998) R16016–R16019.
[130] H. Kuzmany, Solid-State Spectroscopy: An Introduction, 2nd. Ed, Springer Berlin, Heidelberg, 2009.
[131] A. Lucotti, M. Tommasini, M.D. Zoppo, et al., Chem. Phys. Lett. 417 (2006) 78–82.
[132] P. Marabotti, M. Tommasini, C. Castiglioni, et al., Carbon 216 (2024) 118503.
[133] A. Milani, A. Lucotti, V. Russo, et al., J. Phys. Chem. C 115 (2011) 12836–12843.
[134] J.S. Dhindsa, E.L. Cotterill, F.L. Buguis, et al., Angew. Chem. Int. Ed. 61 (2022) e202208502.
[135] F. Hu, C. Zeng, R. Long, et al., Nat. Methods 15 (2018) 194–200.
[136] H. Tabata, M. Fujii, S. Hayashi, et al., Carbon 44 (2006) 3168–3176.
[137] M. Wanko, S. Cahangirov, L. Shi, et al., Phys. Rev. B 94 (2016) 195422.
[138] S. Yang, M. Kertesz, J. Phys. Chem. A 110 (2006) 9771–9774.
[139] C.D. Tschannen, G. Gordeev, S. Reich, et al., Nano Lett. 20 (2020) 6750–6755.
[140] C.D. Tschannen, M. Frimmer, G. Gordeev, et al., ACS Nano 15 (2021) 12249–12255.
[141] A. Cupolillo, M. Castriota, E. Cazzanelli, et al., J. Raman Spectrosc. 39 (2008) 147–152.
[142] Á. Rusznyák, V. Zólyomi, J. Kürti, et al., Phys. Rev. B 72 (2005) 155420.
[143] A. Tapia, L. Aguilera, C. Cab, et al., Carbon 48 (2010) 4057–4062.
[144] S. Heeg, L. Shi, L.V. Poulikakos, et al., Nano Lett. 18 (2018) 5426–5431.
[145] K. Sharma, N.L. Costa, Y.A. Kim, et al., Phys. Rev. Lett. 125 (2020) 049901.
[146] W.Q. Neves, R.S. Alencar, R.S. Ferreira, et al., Carbon 133 (2018) 446–456.
[147] N.F. Andrade, A.L. Aguiar, Y.A. Kim, et al., J. Phys. Chem. C 119 (2015) 10669–10676.
[148] X. Yang, C. Lv, Z. Yao, et al., Carbon 159 (2020) 266–272.
[149] M. Wang, S. Lin, Sci. Rep. 5 (2015) 18122.
[150] C.Z. Wang, C.T. Chan, K.M. Ho, Phys. Rev. B 42 (1990) 11276–11283.
[151] E. Hückel, Z. Angew. Phys. 70 (1931) 204–286.
[152] P.W. Fowler, N. Mizoguchi, D.E. Bean, et al., Chem. Eur. J. 15 (2009) 6964–6972.
[153] Z. Liu, T. Lu, Q. Chen, Carbon 165 (2020) 468–475.
[154] M.N. Glukhovtsev, B.Y. Simkin, V.I. Minkin, Aromaticity and Antiaromaticity: Electronic and Structural Aspects, 1st Ed, Wiley, New York, 1994.
[155] T.M. Krygowski, M.K. Cyrański, Tetrahedron 55 (1999) 11143–11148.
[156] I. Rončević, F.J. Leslie, M. Rossmannek, et al., J. Am. Chem. Soc. 145 (2023) 26962–26972.
[157] T.M. Krygowski, M.K. Cyrański, Chem. Rev. 101 (2001) 1385–1420.
[158] G.V. Baryshnikov, R.R. Valiev, A.V. Kuklin, et al., J. Phys. Chem. Lett. 10 (2019) 6701–6705.
[159] N.D. Charistos, A. Muñoz-Castro, Phys. Chem. Chem. Phys. 22 (2020) 9240–9249.
[160] M. Li, Z. Gao, Y. Han, et al., Phys. Chem. Chem. Phys. 22 (2020) 4823–4831.
[161] Y. Jiang, Y. Wu, J. Deng, et al., Phys. Chem. Chem. Phys. 23 (2021) 8817–8824.
[162] Z. Liu, T. Lu, Q. Chen, Carbon 165 (2020) 461–467.
[163] B. Shi, L. Yuan, T. Tang, et al., Chem. Phys. Lett. 741 (2020) 136975.
[164] M.Z. Rahman, T. Edvinsson, J. Mater. Chem. A 8 (2020) 8234–8237.
[165] S. Hussain, H. Chen, Z. Zhang, et al., Chem. Commun. 56 (2020) 2336–2339.
[166] S.E. Muller, A.K. Nair, Comput. Mater. Sci. 159 (2019) 187–193.
[167] D.M. Guldi, H. Nishihara, L. Venkataraman, Chem. Soc. Rev. 44 (2015) 842–844.
[168] M.B. Nielsen, F. Diederich, Chem. Rev. 105 (2005) 1837–1868.
[169] M. Gholami, R.R. Tykwinski, Chem. Rev. 106 (2006) 4997–5027.
[170] A. Moneo, A. González-Orive, S. Bock, et al., Nanoscale 10 (2018) 14128–14138.
[171] F. Yang, Z. Zheng, Y. He, et al., Adv. Funct. Mater. 31 (2021) 2104254.
[172] S.V. Morozov, K.S. Novoselov, M.I. Katsnelson, et al., Phys. Rev. Lett. 100 (2008) 016602.
[173] F. Yang, Z. Zheng, Z. Lin, et al., Sens. Actuator. B: Chem. 316 (2020) 128200.
[174] S. Kavokina, V. Samyshkin, J. Cao, et al., Nanomaterials 14 (2024) 56.
[175] Z. Zhao, H. Su, P. Zhang, et al., J. Mater. Chem. B 5 (2017) 1650–1657.
[176] A.D. Scaccabarozzi, A. Milani, S. Peggiani, et al., J. Phys. Chem. Lett. 11 (2020) 1970–1974.
[177] S. Pecorario, A.D. Scaccabarozzi, D. Fazzi, et al., Adv. Mater. 34 (2022) 2110468.
[178] W. Xu, E. Leary, S. Hou, et al., Angew. Chem. Int. Ed. 58 (2019) 8378–8382.